Radio Nachweis am Südpol

Diplomarbeit

vorgelegt von

Tilmann Andreas Schultes

Geb. am: 17.06.1983 in Haan

Wuppertal, den 17. August 2010

Gutachter: Prof. Dr. Klaus Helbing

WU D 10-16

Zusammenfassung

Radio-Nachweis am Südpol

Diese Arbeit beschreibt die Entwicklung und Untersuchung eines speziellen Antennentyps zum Nachweis von Radiostrahlung am Südpol. Bei diesem Antennentyp handelt es sich um eine zylinderförmige Dipolantenne, die für ein breites Frequenzband von 25MHz bis 150MHz ausgelegt ist. Der eigentliche Zweck dieser Antennen ist der Nachweis von Radiostrahlung aus Luftschauern. Die meisten Luftschauer werden durch hochenergetische Teilchen erzeugt, welche mit einem Molekühl in der Erdatmosphäre wechselwirken. Der Ursprung der hochenergetischen Teilchen liegt zumeist außerhalb unseres Sonnensystems. Sie gehören zur kosmischen Strahlung, die erstmals 1912 von Victor Hess entdeckt wurde. Bis heute ist die kosmische Strahlung nicht vollkommen verstanden. Ursprung, Ausbreitung, Zusammensetzung und Beschleunigung sind Fragestellungen heutiger Forschung. Durch genaues Messen des Energiespektrums dieser Strahlung sollen Fragestellungen der kosmischen Strahlung überprüft werden.

In den Luftschauern entstehen relativistische Elektronen die durch das Erdmagnetfeld abgelenkt werden und dabei kohärente Radiostrahlung im MHz Bereich ausstrahlen. Eine grundlegende Zielsetzung besteht daher im Nachweis dieser Radiostrahlung am Südpol mit hilfe dafür entwickelten Antennen. Allerdings boten sich im Jahr 2009 noch nicht die Möglichkeiten die Antennen mit einem adäquaten Auslöser zwecks Datenname zum Nachweis dieser Strahlung auszustatten. Stattdessen wurde der Untergrund der Radiostrahlung untersucht, um mögliche Störquellen zu identifizieren.

Das erste Kapitel dient zur Einführung der kosmischen Strahlung, der Physik von Luftschauern und der Emission von Radiostrahlung aus Luftschauern ein.

Das zweite Kapitel behandelt die Antenneneigenschaften und beschreibt den Aufbau der zylinderförmigen Dipolantennen.

Das dritte Kapitel wertet die Messdaten von 2009 aus. Zuerst werden die Eigenschaften der Datennahme beschrieben. Darauf folgt die Untersuchung

von den Eigenschaften der Messdaten. Hier werden unter anderem die Signale in der Zeitdomaine hinsichtlich der quadratischen Abweichung vom Mittelwert untersucht.

Im vierten Kapitel wird eine Schwankung im quadratischen Mittelwert diskutiert, die eine Periode von einen Tag minus 4 Minuten aufweist. Als Ursache für diese Schwankung wird eine Quelle außerhalb des Sonnensystems vermutet. Ein Abschattungseffekt zwischen einem Gebäude nahe der Antenne und der Region um das Zentrum der Galaxie wurde festgestellt.

Zuletzt wird noch ein Ausblick auf weitere Verfahren zur Untersuchung der Antenne gegeben.

Contents

Introduction

This thesis is about the research and development on a special antenna type built for measuring radio emission at the South Pole. This special antenna type is a biconical dipole antenna, which is designed for a broad frequency band ranging from 25MHz to 150MHz. The initial purpose for this antenna type is the proof of radio emission of air showers. Most air showers are created by collision of high energetic particles - coming from far beyond the solar system - with the Earth's atmosphere molecules. These particles are part of the cosmic radiation, which was discovered by Victor Hess in 1912. Until today, the cosmic radiation has not been fully understood yet. Origin, propagation, composition and acceleration are important topics of today's science and research. The exact measurement of the cosmic ray spectrum should actually prove these according theories.

In air showers electrons are generated, which are bent by the Earth's magnet field and they are emitting coherent radio emission in MHz frequency band. A later goal to be achieved is using this antenna to measure this radiation emitted. In 2009, there also did not exist any possibilities to detect this radio emission because a special trigger for the data acquisition was missing at that time. Instead the background noise was researched to detect possible noise sources.

The first chapter will introduce the cosmic rays, the air showers and the emission of radio radiation from air showers.

The second chapter will be about the antenna features and describes the design of the biconical dipole antenna.

The third chapter will analyze the data, which were recorded in 2009. First the data recording and investigating the features of the data will be described: Among others the features of the standard deviation of waveforms will be discussed.

The fourth chapter will be about the modulation of the standard deviation. This modulation is about 4 minutes shorter than the duration of a normal day. As source for this phenomenon is assumed from far beyond our solar system. A shadowing effect between the building near the antenna and

the region around the galactic center was detected, too.

At last an outlook on further measurements and developments of the antenna will be given.

Chapter 1

Cosmic Rays and Radio Emissions

Cosmic rays are highly energetic particles reaching the Earth from areas far beyond the solar system. But the particles emitted from the sun also belong to the cosmic rays. The understanding of origin and propagation of cosmic radiation have been the focus of research since the last century. The first evidence of cosmic radiation was discovered by Victor Hess in 1912 [1]. In several balloon flights up to 5 km altitude, he measured the intensity of ionized radiation and he detected that the intensity increased by altitude and therefore concluded that the radiation must come from the space and not from the Earth as expected before. For this discovery he was awarded with the Nobel Price in 1936. Later, Werner Kohlhörster [2] extended the measurement up to 9 km in altitude.

In the late 1930s discoveries of signals by Pierre Auger [3] and Werner Kohlhörster [4], which appeared in two detectors several meters apart at the same time, led to the discovery of air showers. Air showers are secondary particles that are created from a primary cosmic ray particle.

Since the 1940s the detection of primary particles have been carried out by balloon or satellites experiments and the detection of secondary particles created by air showers have been researched by ground based experiments. Many experiments have formed our today's view on the composition and spectrum of cosmic rays. For higher energetic particles (several PeV) the flux is too low for direct measurements of the primary particles. This is why only ground based large scale detectors can find them by measuring their secondary particles. Anyway, the reconstruction of the energy and direction of the primary particles is a difficult task, that heavily depends on the used interaction model.

1.1   Cosmic Rays Energy Spectrum

The energy spectrum of the cosmic rays of the average differential flux of non thermal origin is shown in figure 1.1. This energy spectrum ranges remarkably from about few MeV to 10^{20}eV. This spectrum follows a power law:

$$\frac{dN}{dE} \propto E^{\gamma} \tag{1.1}$$

The flux of the spectrum decreases from 1000 particles per second per m^2 at GeV energies to 1 particle per year at PeV energies. At the highest energy range of above EeV, the flux is decreased to 1 particle per century per km^2. Up to an energy $\approx 4 \cdot 10^{15}$eV the spectral index is $\gamma = 2.5$ and than a change happens to $\gamma = 2.7$ at the so-called knee. The knee was first discovered in 1958 [5]. A possible second knee was suggested [6] later. And the so-called ankle, first observed in 1980 [7], indicates a change of the spectral index at an energy about $4 \cdot 10^{18}$eV. A cutoff of the spectrum at $6 \cdot 10^{19}$eV, the so-called GZK cutoff [8] was predicted by Kenneth Greisen, Georgiy Zatsepin and Vadim Kuzmin. The GZK cutoff is a reaction of high energy proton (energy above 10^{20}eV) with a cosmic microwave background photon (discovered 1965 [9]). The reaction equations are:

$$p + \gamma_{CMB} \rightarrow \Delta^+ \quad \rightarrow \quad p + \pi^0 \rightarrow p + \gamma\gamma \tag{1.2}$$
$$p + \gamma_{CMB} \rightarrow \Delta^+ \quad \rightarrow \quad n + \pi^+ \tag{1.3}$$
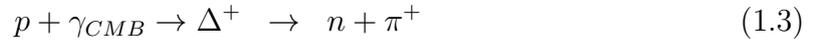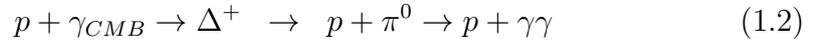
The HIRes [10] and AGASA [11] experiments obtained contrary results for the existence of the GZK cutoff, but Auger expermient confirmed the HIRes result in 2009 [12]. The measurement of this spectrum will help to verify theories of the origins and propagations models of cosmic rays. For higher energy the extensive air showers are the common method to measure these fluxes.

1.2   Extensive Air Showers (EAS)

A high energy cosmic ray particle hits the Earth's atmosphere and initiates an extensive air shower (EAS) of secondary particles cascading down to the ground with nearly light speed. A principle sketch of an EAS is shown in figure 1.2.

In most cases the first interaction of a hadronic primary particle is a hadronic interaction with a N_2 nitrogen or an O_2 oxygen molecule in the atmosphere. The Earth's atmosphere consists of about 75% N_2 nitrogen
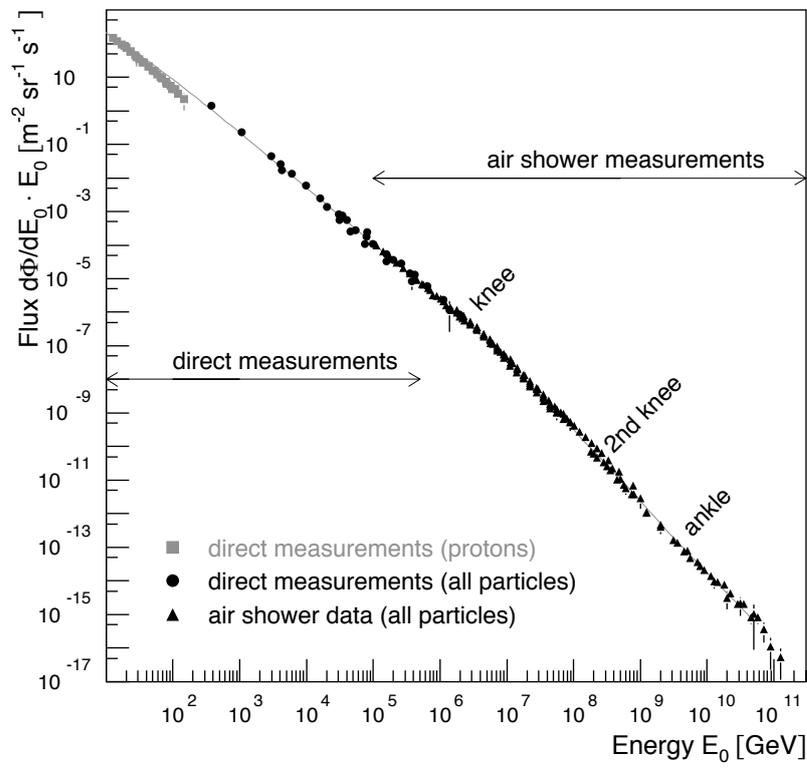
Figure 1.1: All-particle energy spectrum from cosmic rays. (from [13])

molecules and about 23% O_2 oxygen molecules. This interaction produces mostly pions, kaon and nucleons. The neutral pion decay feeds the electromagnetic shower component and the charged pions and kaons interact with air molecules or decay into muons. Apart from hardronic primaries, the shower can also be induced by a photon or lepton. The hadronic components are almost negligible for these showers.

To describe the longitudinal shower development, the atmospheric slant depth has to be introduced first. This depth does not depend on the atmospheric density profile. It describes transversed mater in g/cm^2. In addition, the Gaisser-Hillas function [14] describes the longitudinal shower development of the number of particle count $N(X)$ at a given atmospheric slant depth X , where N_{max} is the maximal particle shower size at X_{max}. X_{max} and X are given in units of atmospheric slant depth:

$$N(X) = N_{max}\left(\frac{X - X_0}{X_{max} - X}\right)^{\frac{X_{max} - X}{\Lambda}} \exp^{\frac{X_{max} - X}{\Lambda}} \tag{1.4}$$

The parameters X_0 and Λ are shower shape parameters.

1.2.1 Components of EAS

Actually the shower consists of four components:

The hadronic component consists of baryons, nucleons (protons and neutrons) and mesons (pions and kaons).

The muonic component is the result of the decay of charged mesons.

The electromagnetic component consists of photons, electrons and positrons.

The neutrino component consists of neutrinos produced by weak interactions during the shower development.

The shower is propagating along the shower axis. The shower axis is given by the flight direction of the primary particle. All secondary particles scatter away from the shower axis. The muon component scatters much less than the electromagnetic component. The shower resembles a cone with a moving front on its bottom.

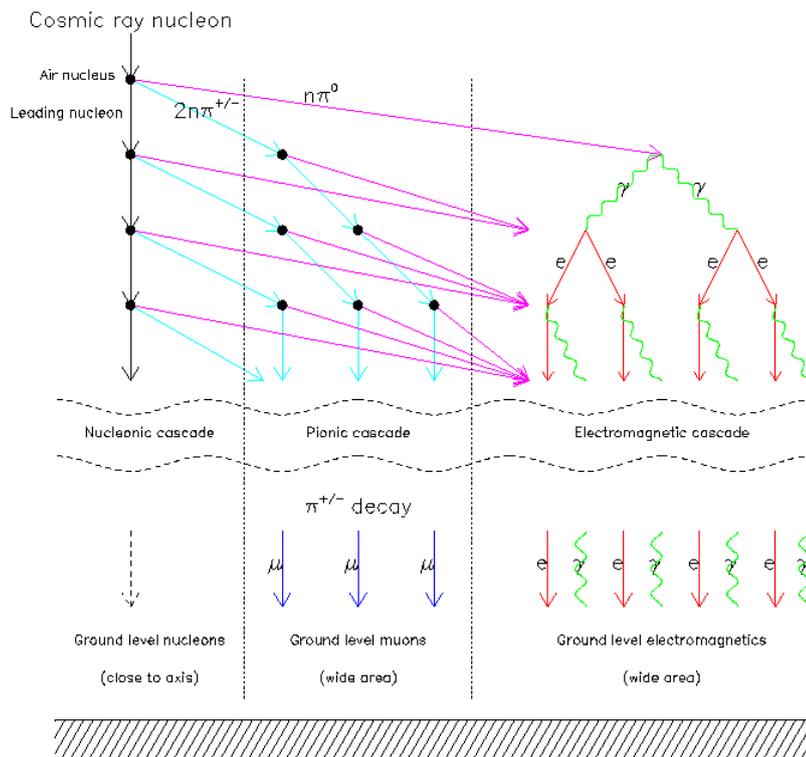The above-mentioned components will now be discussed as follows:

Figure 1.2: The schematic diagram of an EAS was induced by a nucleon. (from [15])

Hadronic component

The hadronic component consists of baryons, mesons and nucleons. In early stages of the shower the hadronic component is dominant, but during the shower development the other components are increasing steadily. On ground level only 1% of the shower components detected are hadronic. Most of the particles are converted into the muonic and electromagnetic components.

Muonic component

In case that the mesons do not interact with air molecules, they decay into lighter mesons or leptons. Most of the mesons have extremely short lifetimes (e.g. 10^{-17}s for a π_0).The most frequent mesons decay reactions occur with their branching ratio (BR):

$$\pi^{\pm} \to \mu^{\pm} + \nu_{\mu}(\overline{\nu_{\mu}}) \qquad\qquad (BR\ 99.99\%)$$
$$K^{\pm} \to \mu^{\pm} + \nu_{\mu}(\overline{\nu_{\mu}}) \qquad\qquad (BR\ 64\%)$$
$$\to \pi^{0} + \pi^{\pm} \qquad\qquad (BR\ 21\%)$$
$$\to 3\pi^{\pm} \qquad\qquad (BR\ 5\%)$$
$$\to \pi^{0}\mu^{\pm} + \nu_{\mu}(\overline{\nu_{\mu}}) \qquad\qquad (BR\ 3\%)$$

Most decay reactions produce muons.

The lifetime of a muon is $\tau = 2.2 \cdot 10^{-6}$s, so it can reach the ground level under the effect of time dilation when it moves with relativistic speed. The higher mass of a muon results in a larger mean free path length compared to that of an electron. The larger mean free path length is used to distinguish between electrons and muons by filtering the electrons using a shielding material (e.g. iron or a thick ice cap).

Muons can lose their energy by ionization and bremsstrahlung, pair production and photo nuclear interactions. Low energy muons from late shower development feed the electromagnetic component of the shower and high energy muons reach the ground and will have lost about 2 GeV as result of ionization, if a muon production high of 15 km is assumed [16] [17].

Electromagnetic component

About 90% of shower components at ground level are electromagnetic. The electromagnetic component is created by a cascade of electromagnetic interactions like pair production and bremsstrahlung. The cascade stops if the produced particles reach a certian energy threshold ($80MeV$ for air). From

then on the energy loss of the particles is caused mostly due to ionization. The number of particles decreases exponentially as described by the Gaisser-Hillas equation 1.4, which is proportional to $N \sim \exp \frac{X_{max} - X}{\Lambda}$.

Neutrino component

Neutrinos are created by weak interactions during the shower development. The neutrinos do not have any charge and are leptons, so electromagnetic interactions and strong interactions are not possible. The neutrinos have a very long mean free path length, so interaction with air molecules are uncommon.

1.2.2 Geosynchrotron radiation

The relativistic electrons and positrons are deflected by the Earth's magnetic field and emit synchrotron radiation.

The synchrotron effect is a combination of the Lorentz force and the radiation of an accelerated charged lepton. A charged lepton q , moving with velocity $\mathbf{v}$, is moving through an external magnetic field $\mathbf{B}$ under the influence of Lorenz force:

$$\mathbf{F} = q(\mathbf{v} \times \mathbf{F}) \tag{1.5}$$

Any accelerated charged lepton emits electromagnetic radiation [18]. In case of acceleration at relativistic energies radiation is emitted in the shape of a forward cone depending on the Lorenzfactor $\frac{1}{\gamma}$.

If this effect is caused by the Earth's magnetic field it is called **geosynchrotron radiation**.

In order to study the geosynchrotron radiation in EAS, two approaches were developed.

An analytical approach developed by Huege & Falcke in 2003 [19] starts with the radiation from a single particle and calculates its radiation emission in the frequency domain.

The vector potential A of an electric field of a moving charge to the unit solid angle Ω can be expressed as:

$$\mathbf{A}(\mathbf{R}, \omega) = \frac{\omega e}{\pi \sqrt{8} c} \exp i \left(\omega \frac{R}{c} - \frac{\pi}{2} \right) [-\hat{\mathbf{e}}_{\parallel} A_{\parallel}(\omega) \pm \hat{\mathbf{e}}_{\perp} A_{\perp}(\omega)] \tag{1.6}$$

where the $+$ sign is used for the electron and the $-$ sign is used for the positron; ω is the angular frequency of the radiation; R is the distance to the observer; the emission is divided into two perpendicular components $\hat{\mathbf{e}}_{\parallel}$ and

$\hat{\mathbf{e}}_{\perp}$. Figure 1.3 demonstrates the geometry of the problem. The electric field can be estimated by the following equation [18]:

$$\mathbf{E}(\mathbf{R}, \omega) = \sqrt{\frac{4\pi}{c}} \frac{1}{R} A(\mathbf{R}, \omega) \tag{1.7}$$

The total emission of the shower can be understood as a superposition of the emission from each charged lepton. Most of the shower particles are concentrated in a slice with 1m thickness, moving along the shower axis. Therefore, the energy spectrum of the radiation is $\propto |\mathbf{A}(\mathbf{R}, \omega)|^2 \propto N^2$ and coherent, where N is the number of charged leptons in the shower at given state. $\mathbf{A}(R, \omega)$ is depending on the frequency, which makes it difficult to integrate it directly over the total shower with respect to the coherency property. The shower is cut into slices at different states and $\mathbf{A}(R, \omega)$ is integrated within these slices.

Another approach to get information on the geosychrotron emission of a shower at different states is the Monte Carlo Simulation with CORSIKA [20]. Figure 1.5 shows the spectrum of the electric field strength for a vertical shower with a primary energy of 10^{17}eV. It also shows that electric field strength loses the coherence and gets numerical noise at higher frequencies for increasing observer distances to the shower center.

Jelley et al. [21] measured the first radio pulses of air showers at 44MHz. They also measured emissions from 2MHz to 520MHz. But until today there has been no reliable comparison of theory and data.

1.3   IceCube Neutrino Observatory

The IceCube Neutrino Observatory, finished in 2011, is a neutrino telescope. A neutrino is not measured directly, instead its interaction product is measured. The principle of the neutrino telescope is the measurement of muons or electrons by Cherenkov radiation in a dense medium. The muon or electron is created by an interaction of a neutrino in a dense medium (ice,rock) around or in the detector. The range of the neutrino in a dense medium depends on the energy of the neutrino and the density of the medium. So far the IceCube detector is a Cherenkov radiation detector in clear ice, 1400 meters below the South Pole surface. This detector will consist of 86 strings, each with 60 photo multipliers equipped. The observed volume of the photo multipliers will be 1km^3. Figure 1.6 shows the IceCube detector.

In addition IceCube has an EAS detector IceTop. The IceTop consists of 2 tanks each attached on the top of every string. Each of these tanks houses two photo multipliers and are connected with the IceCube string. The tanks
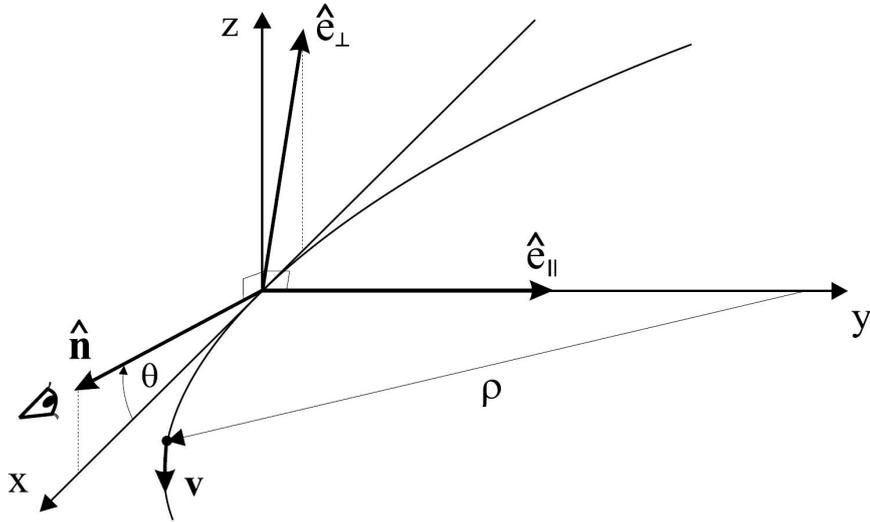
Figure 1.3: The geometry of equation 1.6 for the vector potential of the radiation to a single charged particle. The minus-sign is for a positive charged particle and the plus-sign for a negative charged particle. ρ (about 20km) is the radius of the angular movement. $\hat{\mathbf{e}}_{\parallel}$ and $\hat{\mathbf{e}}_{\perp}$ are perpendicular components of the vector potential. [18] [22]
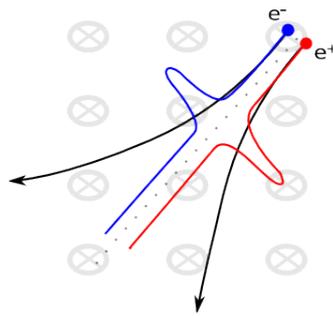

Figure 1.4: A schematic view of the synchrotron emission form an electron and a positron. Both are moving and are deflected in a magnetic field and radiate a short pulse in moving direction of about 10ns in a frequency range of 10 to 150MHz [22]. The red and blue line show the short radio pulses.
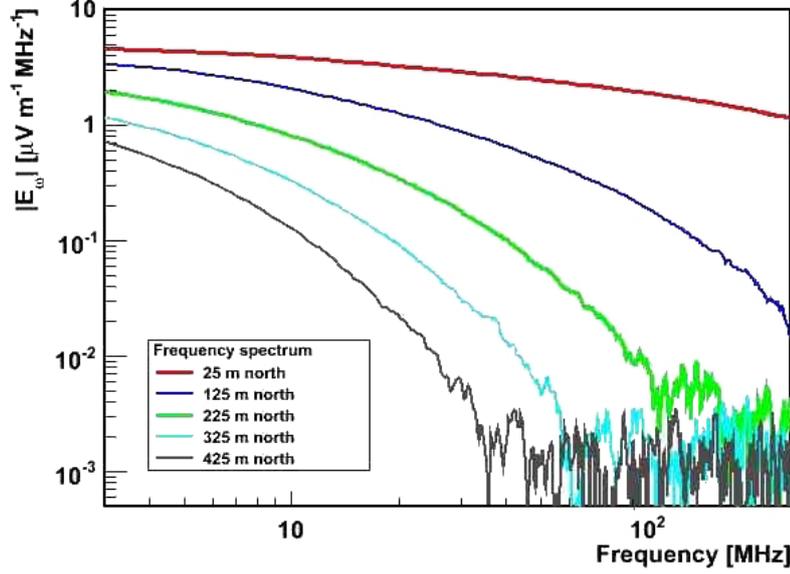
Figure 1.5: Spectrum of the electric field strength of a vertical air shower with a primary energy of 10^{17}eV. It also shows that electric field strength loses the coherence and gets numerical noise at higher frequencies for increasing observer distances to the shower center. (from [22])

measure Cherekov radiation of air shower particles. The purpose of the IceTop detector is to measure the cosmic ray spectrum at its knee. Because the IceTop tanks are 2500m above sea level, the detector can measure at the peak of the shower. The peak means the development stage of the air shower, which has the highest particle count.

The DeepCore of IceCube is in the middle of the IceCube detector and consists of 6 strings, which increase the photo multiplier density in that area. The purpose of the DeepCore is to extend the ability of IceCube to measure lower energy spectrum.

1.4   Radio Air Shower Test Array (RASTA)

The Radio Air Shower Test Array proposal [24] is a 3 year plan for a research and development (R&D) project at the South Pole. The goals of the project are:

- The viability of air-shower detection at the South Pole.

- The study of systematic effects during measurements.

IceCube Lab

50 m

1450 m

2450 m

2820 m

IceTop
80 Stations, each with
2 IceTop Cherenkov detector tanks
2 optical sensors per tank
320 optical sensors

2010: 79 strings in operation
2011: Project completion, 86 strings

IceCube Array
86 strings including 6 DeepCore strings
60 optical sensors on each string
5160 optical sensors

DeepCore
6 strings-spacing optimized for lower energies
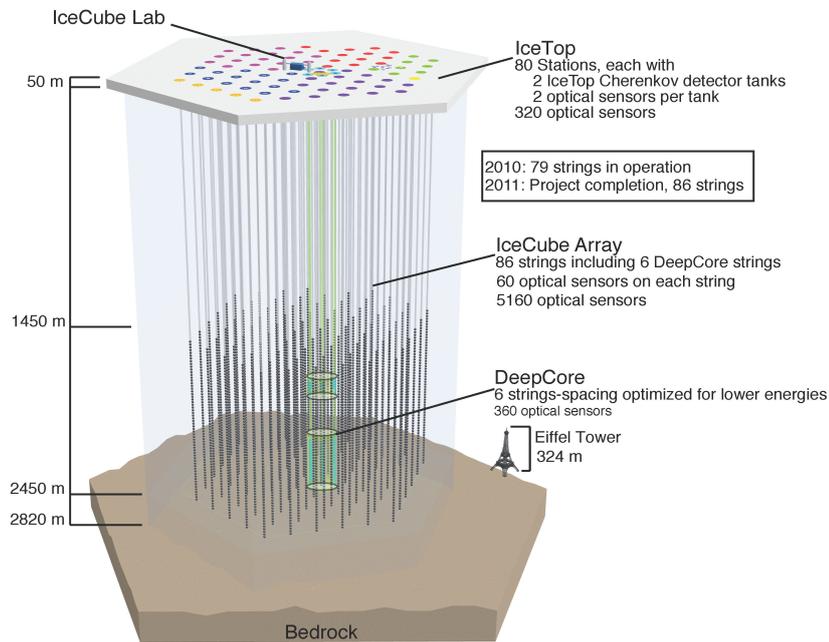360 optical sensors

Eiffel Tower
324 m

Bedrock

Figure 1.6: Current IceCube detector schematic drawing. (from [23])

- Gathering experience in order to build and operate a large scale air shower radio array.

This project can possibly expand the IceCube Observatory in the following ways:

- Increase the detection energy range by increasing the detection size. Radio array is cheaper to build than Cherenkov radiation tanks or scintillators.

- Vetoing muons created by air shower increases the GZK neutrino sensitivity by a factor of three.

- Detection of ultra high energy gamma rays by increasing the detection efficiency using distinction.

For this test array antennas for signal detection of air showers were developed. The first 4 were installed in the beginning of 2009. Two of them are Fat Wire Dipole (FWD) antennas, which are described in this thesis. In the first stage, it is planned to build a small test array of 8 FWD antennas at the South Pole. The next step will be to extend the array with more antennas.

Chapter 2

Antenna

An antenna transmits or receives electromagnetic waves. It converts electromagnetic radiation into an electrical current. Physically, it is an arrangement of one or more conductors. The physics of an antenna are described by the Maxwell Equations.

$$\nabla \mathbf{D} \;=\; \rho \tag{2.1}$$

$$\nabla \mathbf{B} \;=\; 0 \tag{2.2}$$

$$\nabla \times \mathbf{E} \;=\; -\frac{\partial \mathbf{B}}{\partial t} \tag{2.3}$$

$$\nabla \times \mathbf{H} \;=\; \mathbf{J_E} + \frac{\partial \mathbf{D}}{\partial t} \tag{2.4}$$

These equations describe the propagation of electromagnetic wave in the vacuum. For other media the electric field $\mathbf{E}$ and magnetic field $\mathbf{B}$ are defined in relationship with the electric displacement field $\mathbf{D}$ and the magnetizing field $\mathbf{H}$:

$$\mathbf{D} \;=\; \epsilon_0 \epsilon_r \mathbf{E} \tag{2.5}$$

$$\mathbf{B} \;=\; \mu_0 \mu_r \mathbf{H} \tag{2.6}$$

μ_r and ϵ are tensors that describe the magnetic and electric properties of the medium. The current density $\mathbf{J}$ is defined by Ohm's Law:

$$\mathbf{J_E} \;=\; \sigma \mathbf{E} \tag{2.7}$$

2.1 Numerical Electromagnetic Code 2 (NEC2)

The calculation of the electric field with the Maxwell Equations are analytically too difficult for complex antenna geometries, so that a numerical

approach is used. For simulations and calculations of antenna features such as impedance and far field the Numerical Electromagnetic Code (NEC) is used in version 2 [25]. This code uses electromagnetic field integral equations for calculation.

2.2   Antenna features

Some antenna features can be simulated by NEC, will be introduced in the following topics:

2.2.1   Far field

In the far field the relationship between the electric and the magnetic field components is similar to freely propagating waves in free space. The far field begins about 2-3 wavelengths away from the antenna.

2.2.2   Near field

In contrast to the far field, the relationship between the electric and magnetic field component is very complex. The field strength and phase vary in the near field and are strongly depending on their position. Also conducting objects influence the antenna features such as impedance, near field and so on. The near field is the area of one wavelength around the antenna. Between the far field and the near field is a transition zone, which is a mix of both of them.

While objects in the far field can only block signals and do not affect antenna parameters, buildings, conducting ground, wires and so on can affect these parameters in the near field.

2.2.3   Impedance and VSWR

The efficiency between the transmission line and the propagation medium depends on the impedances of an antenna. The transmission line connects the sending or receiving system with the antenna. The impedance of the antenna can be calculated by a simulation. However other elements in the near field range of the antenna change its impedance, too. These elements can be simulated by NEC. NEC can also simulate a plane ground below the antenna. An important point is matching the transmission line impedance to the impedance of the antenna. The matching is done by electric circuits

or designing the antenna impedances equal to the of the cable. An example for impedance matching is a Balun circuit[1]. A mismatch will result in standing waves on the transmission line. The impedance is frequency dependent, which leads to a restricted frequency band in which the antenna is well matched.

The **voltage standing wave ratio** (VSWR) is used to express the matching of the impedance to the antenna for a single frequency. It is defined by:

$$VSWR = \frac{1 + |\Gamma|}{1 - |\Gamma|} = \frac{|Z_a + Z_c| + |Z_a - Z_c|}{|Z_a + Z_c| - |Z_a - Z_c|} \tag{2.8}$$

where Γ is the complex reflection coefficient; Z_a is the impedance of the antenna; Z_c is the impedance of the cable. An ideal match of the impedance will result in a VSWR of 1. If the cable does not match, the VSWR will increase and the result is a standing wave on the signal on the cable.

An alternative definition of the VSWR is by the maximum and minimum voltage from the standing wave on the cable.

$$VSWR = \frac{V_{max}}{V_{min}} \tag{2.9}$$

Another problem is the fact that the simulated results do not fit into the measured results in case that the surrounding objects are not determined exactly. The objects can interact with the near field and change the impedance.

2.2.4 Direction Pattern

An antenna pattern is a representation of the far field radiation of the antenna as a function of direction. There exist representations of the magnetic field (H-plane pattern) and the electric field (E-plane pattern) as antenna patterns. A combination of these fields is the antenna power pattern, which is a representation of the Poynting vector:

$$\mathbf{P} = \mathbf{E} \times \mathbf{H} \tag{2.10}$$

The absolute power pattern is defined as the power density by a given distance in W/m^2. The relative power pattern is defined by the difference to an arbitrarily chosen maximum.

---

[1]Balun = balanced unbalanced circuit transforms an unbalanced signal to a balanced signal and vice versa. Also, often used for impedance matching.

2.2.5   Gain

Antenna gain is the ratio of the maximum radiation in a given direction compared to intensity to an isotropic radiator. This ratio can be expressed by:

$$G = \frac{P_{max}}{P_{iso}} \tag{2.11}$$

where P_{max} is the radiation density of the antenna in its main radiation direction and P_{max} is the radiation density of an isotopic radiator in same direction and distance.

2.3   Fat Wire Dipole

For the radio air shower detector at the Geographic South Pole two fat wire dipole (FWD) antennas were used. Figure 2.3 shows an antenna and figure 2.1 gives a schematic drawing the wires of the antenna without the wooden frame. These antennas are biconical dipole antennas. They were chosen because they are able to receive signals in a wide frequency range from 25MHz to 120MHz.

2.3.1   Construction of the FWD

The FWD consists of a wooden frame, a foot point which connects the antenna with the cable and the wires. The wooden frame is built from four wooden plates and wooden beams which keep these plates at a distance. These plates hold the wires. The wooden plates were cut into rings to reduce the weight of the antenna. Figure 2.2 shows a sketch of the wooden frame. The first design of the antenna held the foot components using a plastic tube. Later it was changed to a wooden beam, that was connected rectangularly to the distance keeping wooden beams. At the beginning, the foot point consists of a tube attached with 8 eye bolts that hold the copper wires. This design was changed to using ring terminals mounted on a metal plate instead of the eye bolts. This modification has the advantage of an easier assembly of the wires' connections. The assembly of a wire to an eye bolt is time consuming and gives an undefined connection. This may cause a higher inductance, because the wire is turned around the eye of the eye bolt. The ring terminals can be assembled faster on the wire and are fixed by a screw. This screw is mounted on a plate which is connected to the wooden beam with two long screws. A big advantage is the prefabrication of the wire connections. The copper wires are $1.8mm$ in diameter. In the first design,
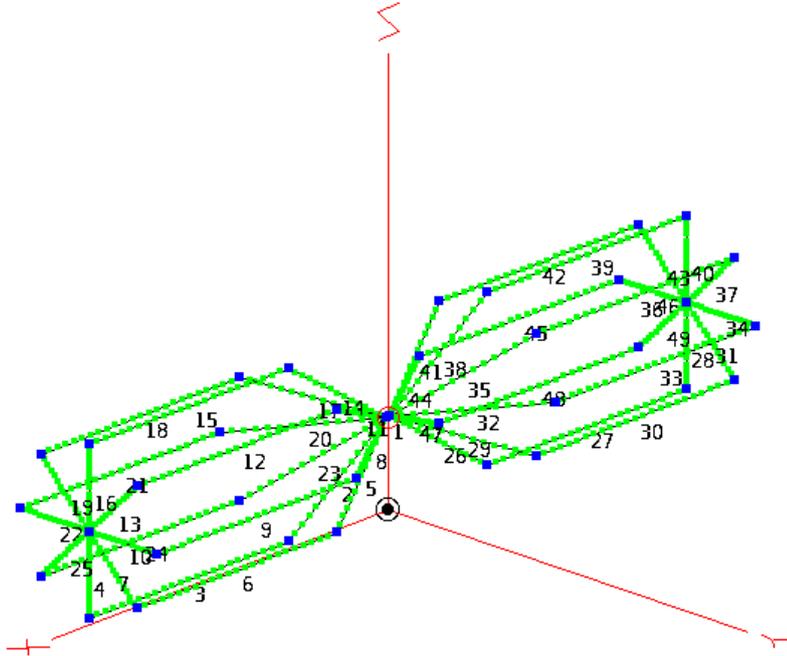
Figure 2.1: Wires of the FWD

the connection to the cable was done by attaching the coaxial cables to the eye bolts. The second design uses a Balun, that is designed for impedance adjustment from 200 Ω to 50 Ω. The foot point is connected to the Balun by a copper wire.

2.3.2 Direction Pattern

The direction pattern of the far field was simulated for different frequencies by NEC. The simulation of the direction pattern is shown in 3D in figure 2.5 and the cuts are shown in figures 2.6 and 2.4. These figures show that the antenna mean beam is about 5 db stronger than the side beam at low frequencies (30-60MHz). At higher frequencies, the patterns show a split of the mean beam. The simulation is done with an ice surface of an $\epsilon_r = 1.7$ [26] and a very low electric conductivity σ.

2.3.3 VSWR

The VSWR was simulated and measured at different locations. NEC simulations were done with different settings like varying the size of the gap between the two foot points, all which effect the VSWR results. The result
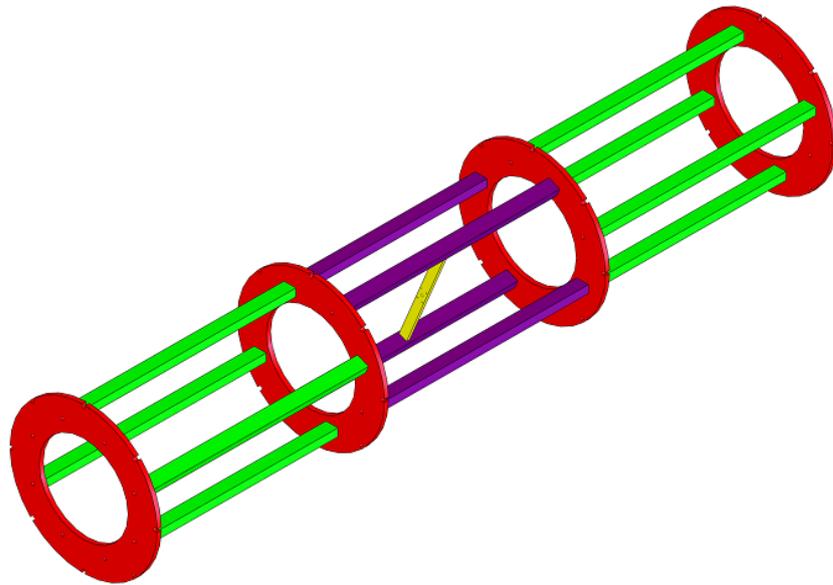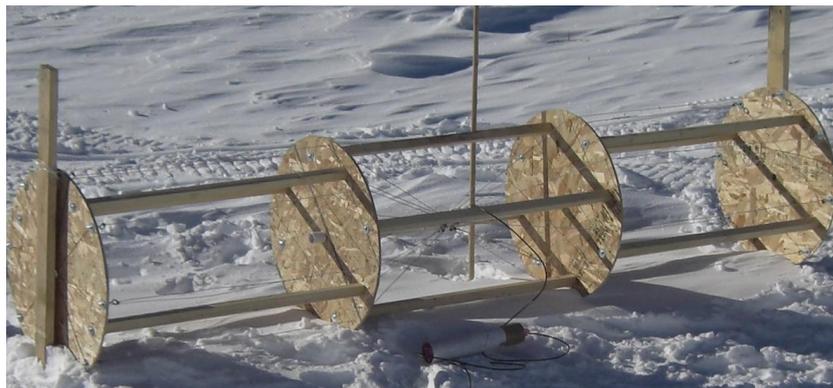
Figure 2.2: Antenna wooden frame

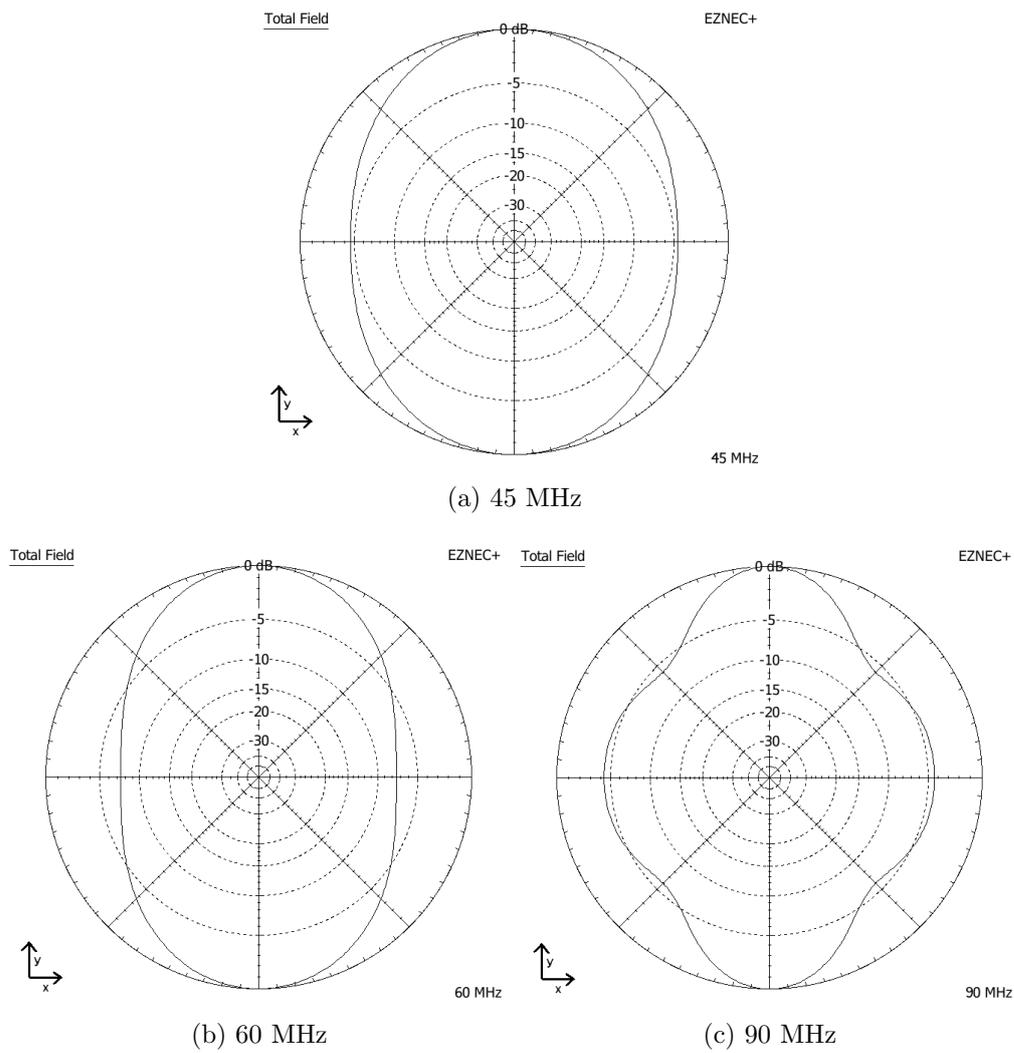Figure 2.3: Picture of one FWD antenna at South Pole

(a) 45 MHz

(b) 60 MHz

(c) 90 MHz

Figure 2.4: Simulated azimuth angle plot of the antenna direction pattern. The plots are calculated at 1° from ground.

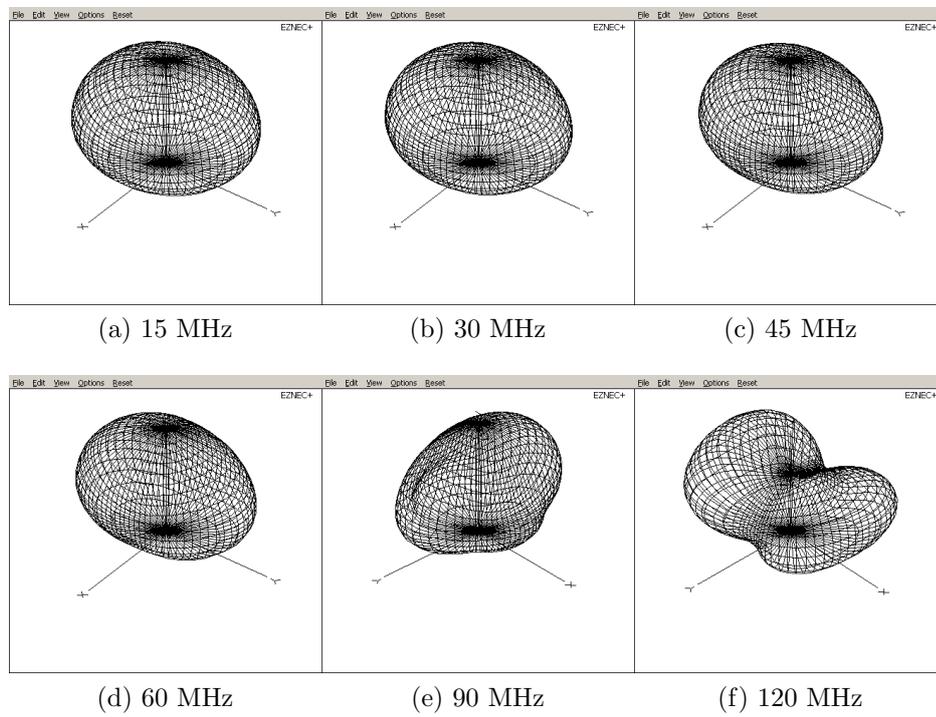(a) 15 MHz   (b) 30 MHz   (c) 45 MHz
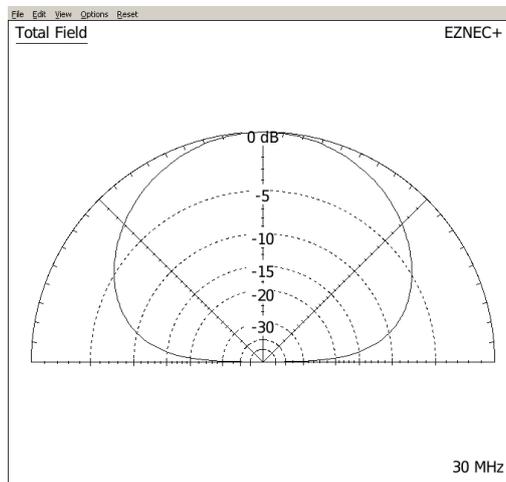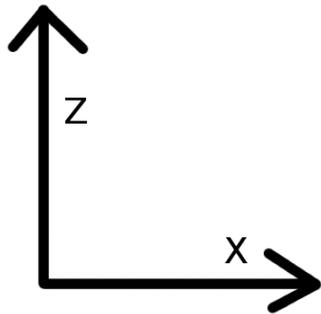
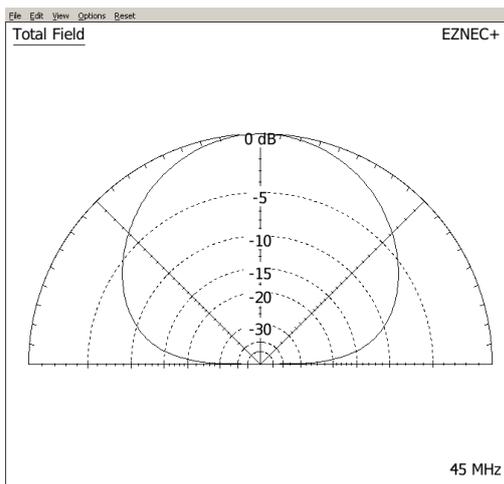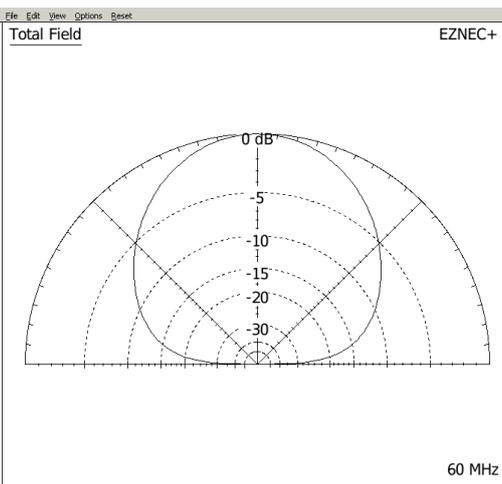(d) 60 MHz   (e) 90 MHz   (f) 120 MHz

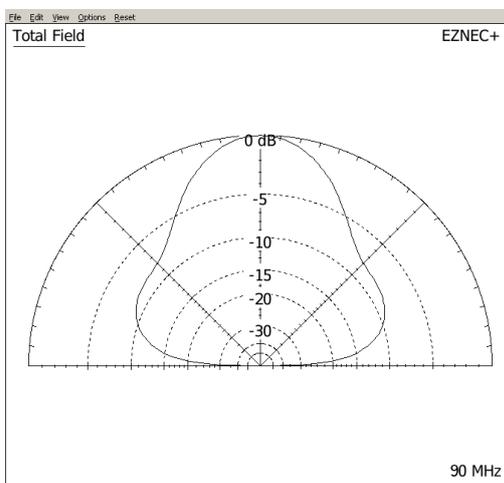Figure 2.5: Simulated 3d plot of the antenna direction pattern.
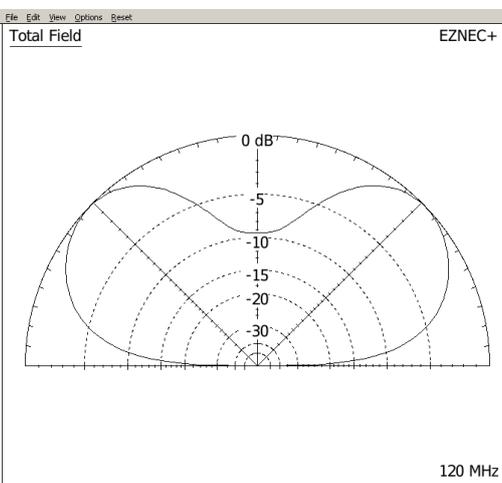
(a) 30 MHz

(b) 45 MHz

(c) 60 MHz

(d) 90 MHz

(e) 120 MHz

Figure 2.6: Simulated elevation angle plot of the antenna direction pattern.
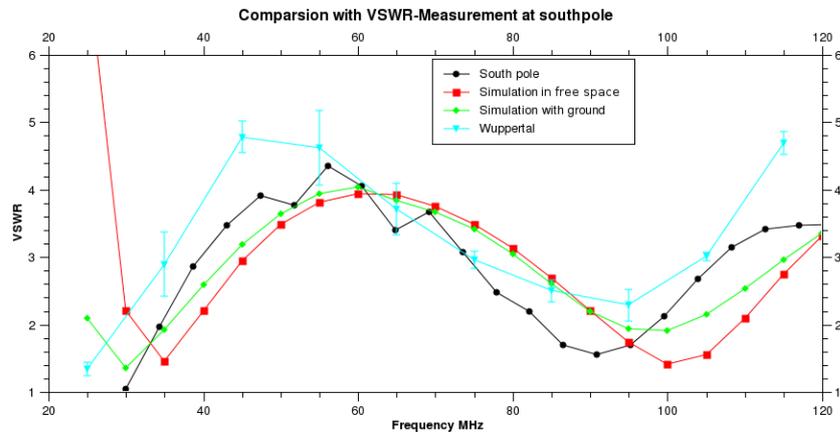
Figure 2.7: Comparison of VSWR measurements with simulations. The black curve shows the South Pole measurement that was taken with the first antenna design in the beginning of 2009. The blue curve shows the mean of four measurements of a prototype antenna design, that was used for comparison measurements. The other two curves are simulations. The systematic error of the South Pole measurement is assumed with 1.

was a larger gap between the foot plates which will further result in a worser VSWR minimum. The size of the antenna changes the position of the minimum. The simulation was also executed for different ground conditions. The result was a shift and a scaling of the VSWR curve. Figure 2.7 shows the simulation of the antenna on a sand surface and in free space and compares it with measurements at South Pole and in Wuppertal. VSWR is below 5 at the frequency range from 25 MHz to 120 MHz. VSWR of 6 means that the signal is reduced by half.

The measurements in Wuppertal were carried out on a mostly free space with objects in the near field. For these measurements the Spectrum Anylizer Tekka Riken TR was used. Figure 2.8 shows the effect when the antenna is turned around the floor.
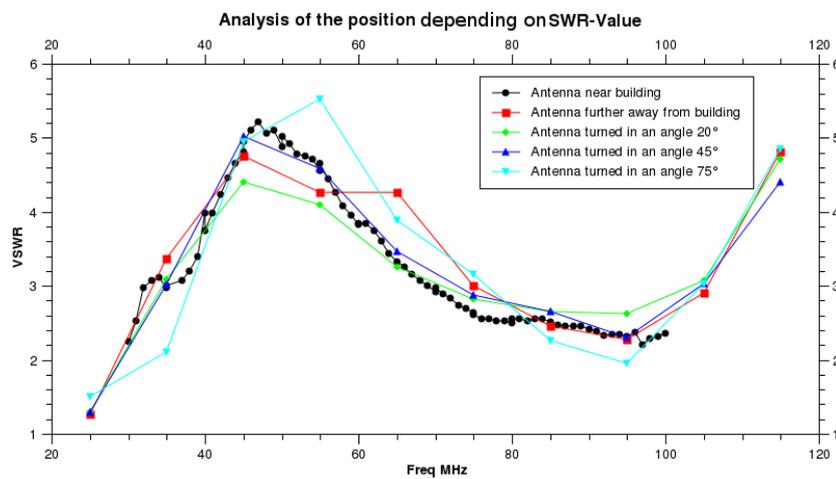
Figure 2.8: Comparison of VSWR of effects by near field objects. The antenna was set by turning at different angels and the VSWR was measured. The variation of VSWR is up to 0.5.

Chapter 3

2009 Data

3.1 Radio in Ice Cherenkov Experiment (RICE)

Radio in Ice Cherenkov Experiment (RICE) has been the first radio Cherenkov detector in the Antarctic Ice for frequencies between 200 MHz and 500 MHz. The detector consists of 18 antennas reaching to a depth between 100 m and 300 m. They are spread in a cube measuring $200x200x200$m^3. Figure 3.1 shows a schematic picture of the RICE detector as well as the Askarayan effect [27].

The so called "Askarayan effect" is the coherent Cherenkov radio emission of charge asymmetry of an electromagnetic shower. Cherenkov radiation is produced when a particle travels faster than light speed in a dense dielectric medium such as sand or ice. The photon-electron asymmetry is created by high energy processes like Compton, Bhabha and Moller scattering and positron-annihilation.

RICE is located in the so-called Dark Sector of the South Pole. In this sector the human made emission of electromagnetic radiation noises (mostly optical due to the telescopes there) is kept as low as possible.

RICE Data Acquisition (DAQ) is located in the Martin A. Pomerantz Observatory (MAPO) building. The DAQ consists of 6 oscilloscopes with 4 channels each with a 1 GHz sampling rate and 12 bit digitization and 8192 samples per waveform. Further it has a trigger logic that sorts out events by threshold and time.In addition it records events every 10 minutes to measure the background.

In 2009 the DAQ uses 22 channels, where 4 channels are for the surface antennas, which are also used as a veto trigger. In 2009, the DAQ uses in all 22 channels with 18 antennas in the ice and 4 antennas on the surface. The DAQ is described in [28] and [22].
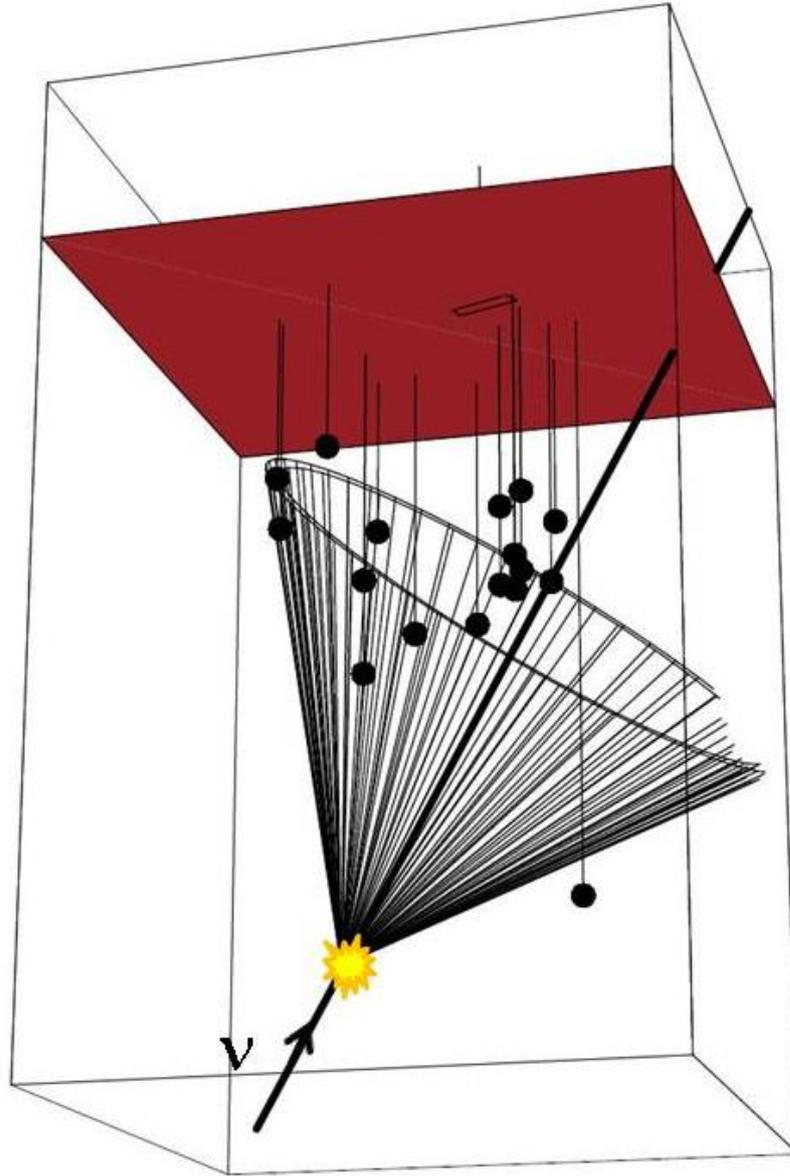
Figure 3.1: RICE schematic picture. The black dots are the 18 in Ice antennas. The rectangle on the red plane is the MAPO building, which houses the DAQ. The front of cone shows a wavefront of Askarayan Cherenkov emission of a lepton induced by a up-going neutrino. (From [22])

3.2 2009 Data

In 2009, 2 Fat Wire Dipole (FWD) antennas and 2 crossed monopoles were attached to the RICE data acquisition (DAQ). Since then, it has been possible to receive a wide spectrum of surface radio signals ranging from 25 to 200MHz at the South Pole.

There does not exist any special trigger for these two FWD antennas. They are triggered by two different trigger types.
The first trigger type is special for RICE purpose and the second type is a self-induced trigger event, which is the so-called minBIAS event. A minBias event defines the dynamic range of the DAQ channels. This event is interesting because it is regularly recorded (every 10 minutes). Further, this event shows the background or coincidentally some other events, too. Chapter 3.3 will describe and classify some minBIAS events.

The data is stored in compressed text files. A description of the file format can be found in [22] Appendix B.

Each file includes several events. An event is stored in the file if the trigger logic has decided so. An event includes several information like time, type of the trigger and the ADC conversion factor. Each event runs up to 22 waveforms which are taken from DAQ channels. A waveform consists of 8192 bins, each bin having a time window of 1 ns.

To achieve fast access to important quantities of the data a ROOT Tree was built. The important quantities are the RMS, the mean of each waveform and general event information. ROOT is a software library for data analysis. A detailed explanation can be found at [29].

The ROOT Tree contents 281760 events which were recorded in 2009.

3.3 Features of the data

An event consists of general information and waveforms with some additional features. The general information consists of trigger type, time, event number and others, which are not interesting for this analysis. The additional waveform features are the ADC conversion factor, the mean and the RMS.

3.3.1 Event type

The event type feature describes the trigger type of the event. Currently we classify the event into 4 classes:

General events are triggered if more than 4 'in ice antennas' receive a signal above threshold.

MinBias events defines the ADC conversion factor. A minBias event is recorded every 10 events or every 10 minutes.

VetoTDC events are sorted out by a time pattern. Generally these are events which come from the surface.

Unknown events are not classified by the software, because the software does not known how to classify these events.

The event distribution is shown in figure 3.2. About 20% of the events are minBias.
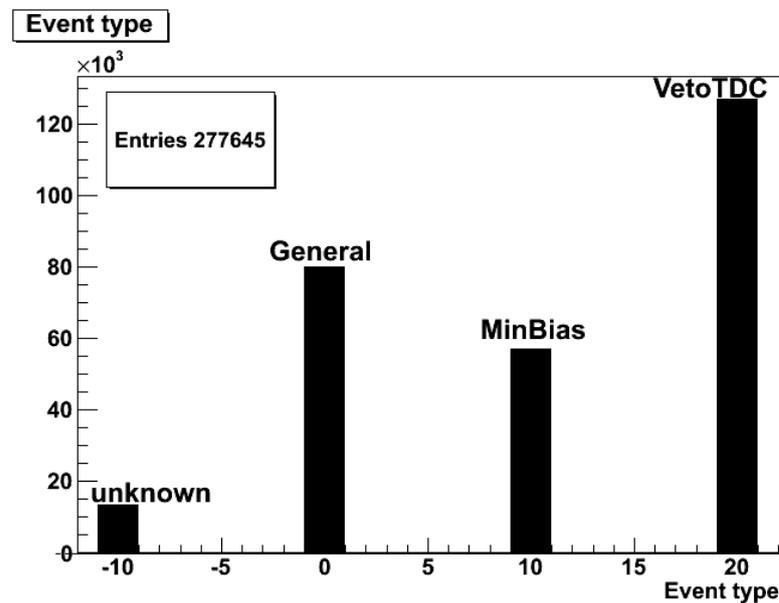
Figure 3.2: Distribution of event type. Most of the events are classified as VetoTDC and general. About 60000 are classified as minBias events. The data for this distribution was created around Christmas, the last week of 2009 is missing.

3.3.2   Event Number

The event number property is an index number. Each process of data collecting creates a new numerical series of index numbers. That process is a so-called run. So each event has an event number which indexes the events during the according run. The event numbers from a run are a numerical series which starts with 1. The increment of the numerical series is 1. Please note these numbers are unique in each run.

Figure 3.3 shows the event number distribution. This event number distribution is interpreted as numerical series stacked as slices, ordered by their size. Most of the numerical series end before 1500.

Slices should not be interrupted, because otherwise the numerical series will be interrupted. If the slices are ordered by theirs sizes, the distribution has the shape of a monotonic decreasing function.

The monotonic decreasing shape is interrupted in figure 3.4, so there is at least a minimum of one numerical series interrupted. This means that from one run some events must be missing. In fact, there are few corrupted files in the RICE dataset, so the result is not surprising. These files are ignored by analysis.

In conclusion, the event number gives a good indication of integrity as to the data derived.

Also, events with the event number '= 1' are interesting because these are events which define the dynamic range of the oscilloscopes.

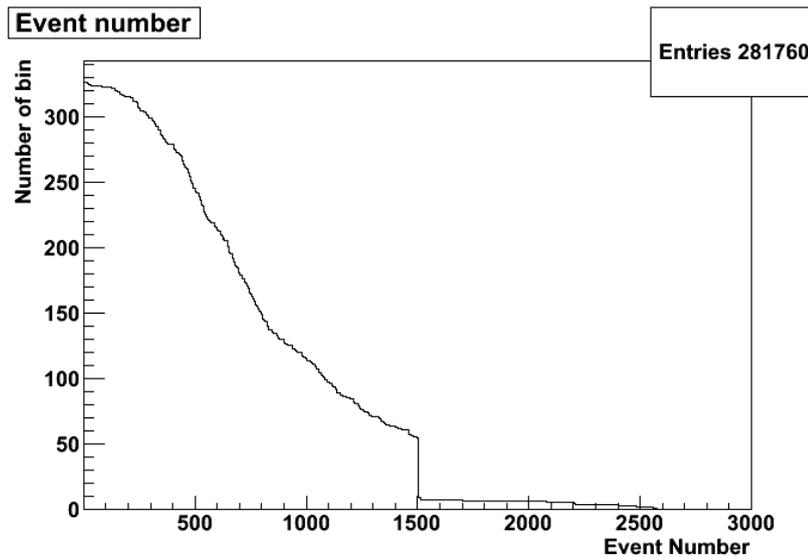Figure 3.3: The distribution of event number. If this is interpreted as numerical series stacked as slices, ordered by their size, than the distribution should have monotonic decreasing function as shape. But figure 3.4 shows that this is not the case.

3.3.3 Waveforms

In a time frame of 8.192 μs, a waveform stores a 12 bit voltage discrete signal of an antenna with a 1 GHz sampling rate. Every event has up to
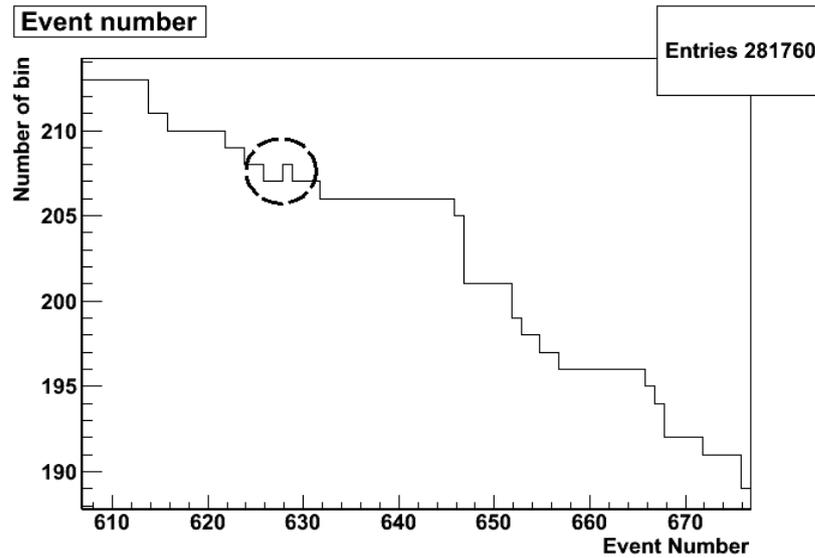
Figure 3.4: The part distribution of an event number gives an indication to an invalid numerical series, if this is interpreted as numerical series, stacked as slices, ordered by their size. The circle shows a violation of the monotonic decreasing function, so that there is a numerical series, seen as slice with a hole and with missing numbers.

22 waveforms, depending on the mode in which the DAQ was operating. In some surface tests only the surface waveforms were recorded.

The waveform data format consists of 4 floating point features values and 8192 12 bit signed integer data values. The 4 features values are time delay, sample rate, offset and ADC conversion factor. The time delay defines the period passed from the trigger to the center of the waveform. The sample rate is on 1 GHz.The offset is zero. The ADC conversion factor is for converting the integer value into a voltage value. The ADC conversion factor has to be multiplied by a factor of 8, whereas the origin of this factor is unknown.

3.3.4   ADC conversion factor

The ADC conversion factor converts the 12 bit integer value of a waveform into a voltage value. It also estimates in which voltage range the waveform was quantized. A wrong dynamic range gives a distortion in quantization.

Research on that factor resulted in an interesting correlation between events with event number equal to 1 and the factor. The DAQ resets the voltage range when a new run of data collection is started. Most of these first events have bad quantized waveforms. Figure 3.5 shows two bad quantized

waveforms.
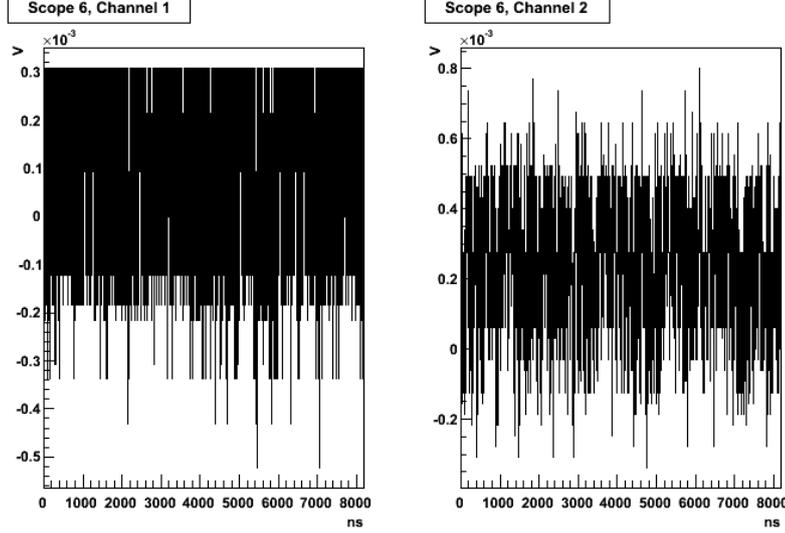
Figure 3.5: Bad quantisated waveforms in SPASE1 (left) and SPASE2 (right) antennas. The waveforms was taken in an unmatched dynamic range of the oscilloscope.

3.3.5 Mean of the waveform voltages

The mean of a waveform is the sum above all voltage values x_i from the waveform, which is divided by its length N:

$$\overline{x} = \frac{1}{N} \sum_{i=1}^{N} x_i \tag{3.1}$$

3.3.6 RMS of the waveform voltages

The root mean square (RMS) is known as the quadratic mean. The RMS of a waveform is the square root sum above all quadratic voltage values x_i from the waveform, which is divided through its length N:

$$\overline{x}_{RMS} = \sqrt{\frac{1}{N} \sum_{i=1}^{N} x_i^2} \tag{3.2}$$

It's especially used for determining a positively and negatively varying quantity, like a sine wave.

Physics often name wrongly standard deviation as RMS, thus many program function calls, which calculate the standard deviation, include RMS in their names.

3.3.7   Standard deviation of the waveform voltages

The standard deviation is the quantity given for variability. The standard deviation σ is the square root sum above all quadratic voltage values x_i difference to its mean $\overline{x}$, which is divided through its length N:

$$x_\sigma = \sqrt{\frac{1}{N} \sum_{i=1}^{N} (x_i - \overline{x})^2} \qquad (3.3)$$

In contrast to the RMS, the standard deviation gives a RMS with an eliminated offset. So we have a good idea of the size of a positive/negative varying quantity. This makes it to an important factor to classify the waveform. The standard deviation is in relation to RMS and mean shown in equation as follows:

$$x_\sigma^2 = \overline{x}_{RMS}^2 - \overline{x}^2 \qquad (3.4)$$

The distribution of the standard deviation data of SPASE1 antenna is shown in figure 3.6. The distribution is shown in a stacked histogram of minBias events. Different event classes exist.

The first class of events is the missing waveform class; all these events have missing waveforms. A missing waveform can be caused by a pinger run. A so-called 'pinger run' will be explained later in chapter 3.4.2. There is no evidence that these events change the distribution of standard deviation.

The second class is the event 'number equal to one class', with event number '= 1'. These events have event numbers equal to one. They have bad quantized waveforms that mostly show the same standard deviation.

The third class is the VLF class, which is explained in chapter 3.4.1. These events have a big impact on the distribution of standard deviation.

All other events are part of the not classified class.

The distribution of SPASE1 antenna, which is shown in 3.6, shows three peaks.

The first peak is caused by a dismantling of the antenna in November of 2009, so there is not any antenna gain of radio signals anymore.

The Second peak is the normal background signal form the minBias events.

The third peak shows bad quantized waveforms peaks which are caused by wrong threshold values in the DAQ.

The distribution of SPASE1 antenna is also shown in figure 3.7, every day of the year. In this figure a signal drop due to dismantling of the antenna at the end of 2009 can be seen. Another effect is the signal strength drop at about 130 day in SPASE1 antenna, here is assumed that the connection get worser.

In figure 3.9 the distribution of the SPASE2 antenna shows an additional peak, which might have been caused by connection problems. A possible source for this problem could be the connections of the antenna wires of the first antenna design, which have resulted in a changed impedance of the antenna. This change could stem from some certain weather conditions.
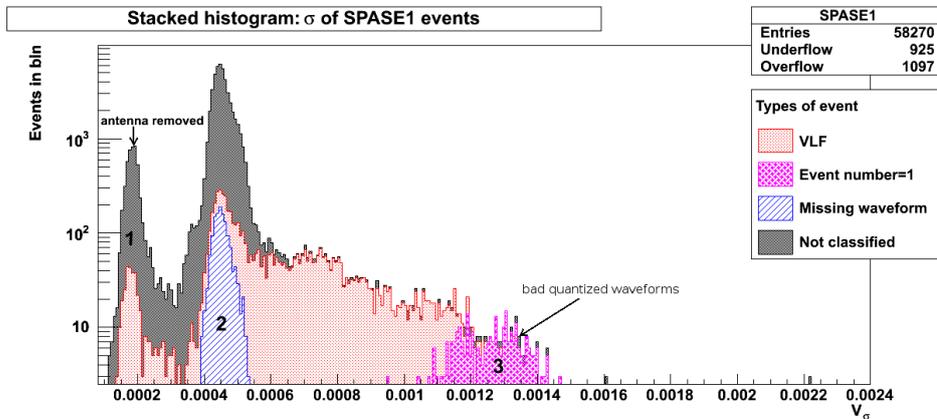

Figure 3.6: A stacked histogram of distribution of standard deviation of the minBias event waveforms. The event are classified in four different classes. The interesting types are 'event number equal to one' and VLF, because these have an effect on the distribution(3). Further, the dismantling of the antenna in November 2009 can be seen in the distribution as a Gaussian peak(1) on a lower voltage level. Most of the unclassified events can be found in the center peak(2). Some of the events are out of the range of the graph, but most of them are VLF events.

3.4 Recorded events

Apart from the normal background noise the occurrence of signals from various devices is received by the surface antennas. Three experiments, carried out at the South Pole, could be found in the data as well.

The first is the Very Low Frequency (VLF) Beacon which has been the biggest source for unwanted signals.

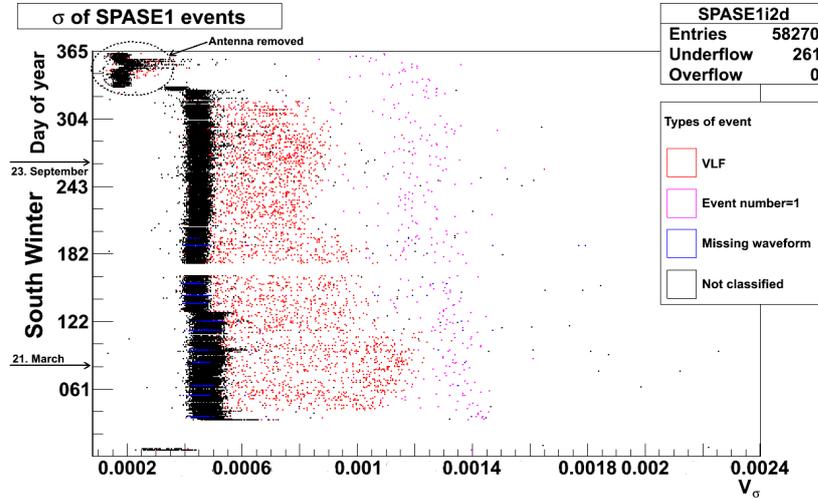Figure 3.7: Distribution of the Sigma of the SPASE1 antenna in a 2D histogram on every day in 2009. Until about day 120, the signal strength is stronger, than it drops. At the end of the year the antenna was removed.
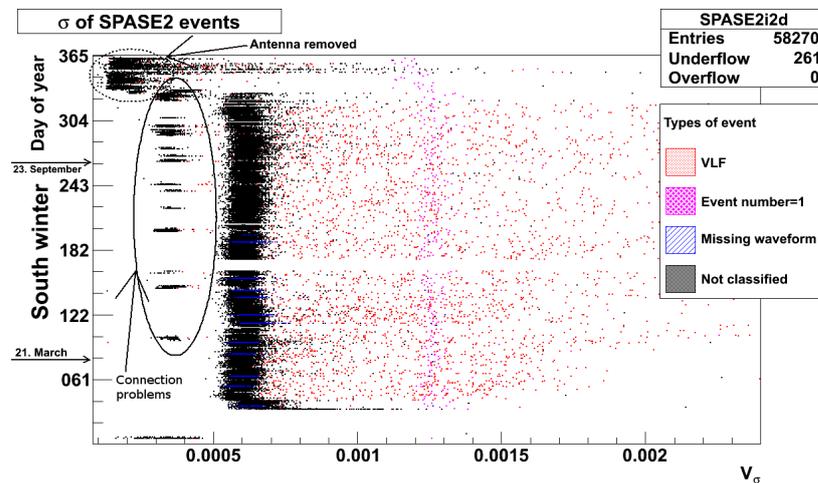

Figure 3.8: The distribution of the Sigma of the SPASE2 antenna in a 2D histogram for every day in 2009. Possible connection problems were seen in 2009. At the end of the year the antenna was removed.
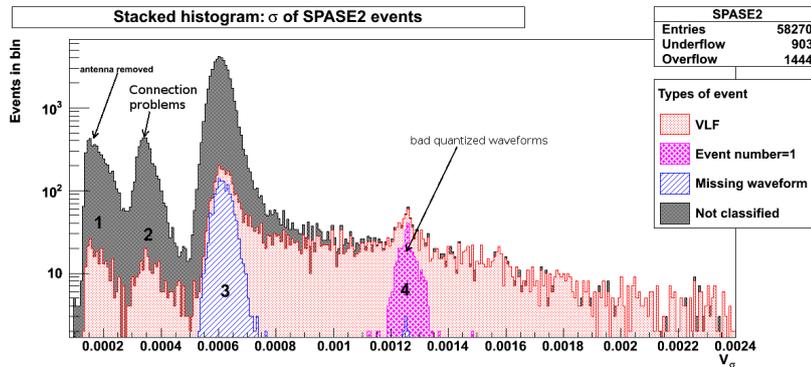
Figure 3.9: A stacked histogram of the distribution of the standard deviation of the minBias event waveforms. The events are classified in four different classes. The interesting types are 'event number equal to one' and VLF, because these have an effect on the distribution. Also the dismantling of the antenna in November 2009 can be seen in the distribution as a Gaussian peak(1) on a lower voltage level. The SPASE2 antenna has also some problems with its connections(2). Some of the events are out of the range of the graph, but most of them are VLF events.

The second source is the 'pingerrun' test, which proves the surface antennas' ability to relocate the source of the signal.

The third is the meteor radar which is also unwanted but does not occur often.

3.4.1 Very Low Frequency Beacon Signals (VLF)

At the South Pole the Standford Very Low Frequency Beacon exists which investigates questions concerning the lower ionospheric and mesospheric signatures [30] [31]. These ionospheric signatures are measured via their effects on a very low frequency signal. This signal is transmitted from a 7 km long beacon antenna and received at various Antarctic locations.

This antenna transmits a 60 seconds lasting signal ranging from 19.350kHz to 19.500kHz every 15 minutes. The first 2 seconds of the signal are in Morse code "NPX". The code is sent by frequency shifts of 19.400kHz and 19.500kHz [32].

The SPASE antennas have a high-pass filter with 25 MHz near the antenna, so that the antenna itself does not transmit the signal to the DAQ. Instead the cable receives the signal and acts as an antenna for low frequency signals. In figure 3.12 is shown that the SPASE antenna cables run parallel to the beacon antenna, which makes them a good antenna for these signals.

These signals were also received when the antennas were removed.

A sample of a received signal is shown in 3.13. Such a signal creates a wide range of standard deviation values as seen in 3.6 and 3.9. A special filter has been developed for sorting out these signals. This filter cuts out every signal which is in the VLF sending time window. The VLF sends during 60 seconds every hour in minute 6, 21, 37 and 51.
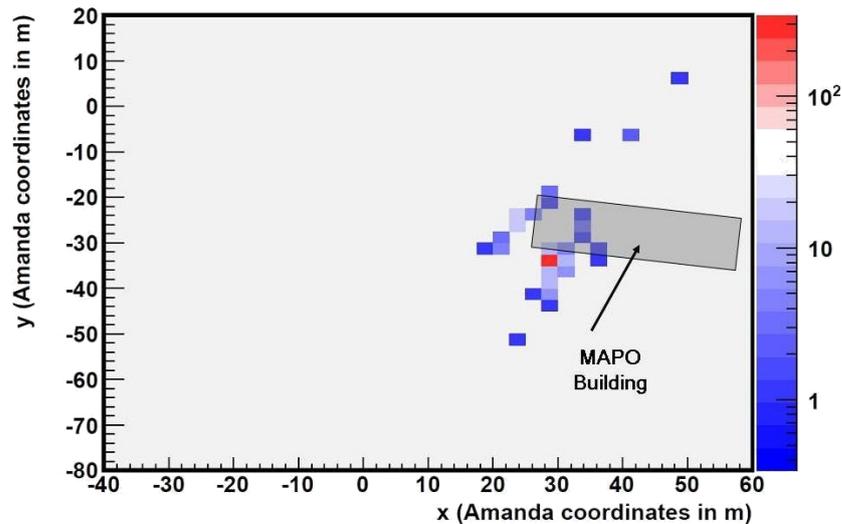

Figure 3.10: Result of the 'Pingerrun's events reconstruction done by Jan Auffenberg [22]. The result of the reconstruction of 'Pingerrun' events will be discussed here. The GHz horn antenna (red dot) is located at the MAPO building and was successfully located by the SPASE antennas.

3.4.2   Pingerruns

Another study was carried out to prove the time and 3D reconstruction of events [22]. This study used a GHz horn antenna near the MAPO building. This horn antenna was sending signals which were received by the SPASE antennas. This sending process was called 'Pingerrun'.

In a 'Pingerrun' only the oscilloscopes with attached surface antennas were receiving data. So these 'Pingerruns' could also be easily identified because they have but 6 waveforms instead of 22. Figure 3.11 shows the 'Pingerun' signal and figure 3.10 shows the event reconstruction from Jan Auffenberg's doctor thesis [22].

In Figure 3.7 and 3.8 the blue dots represent the 'Pingerruns'; they match with the notes of the AURA pole log book [33]. Table 3.1 compares the data
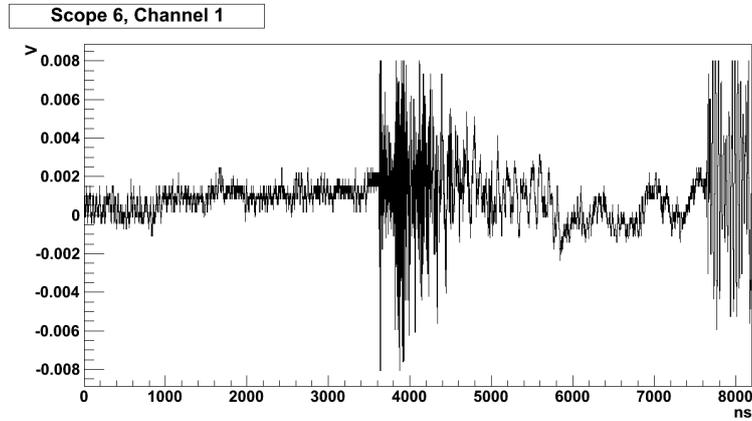
Figure 3.11: Waveform of a 'Pingerrun' event with the 'Pingerrun' signal in the center.
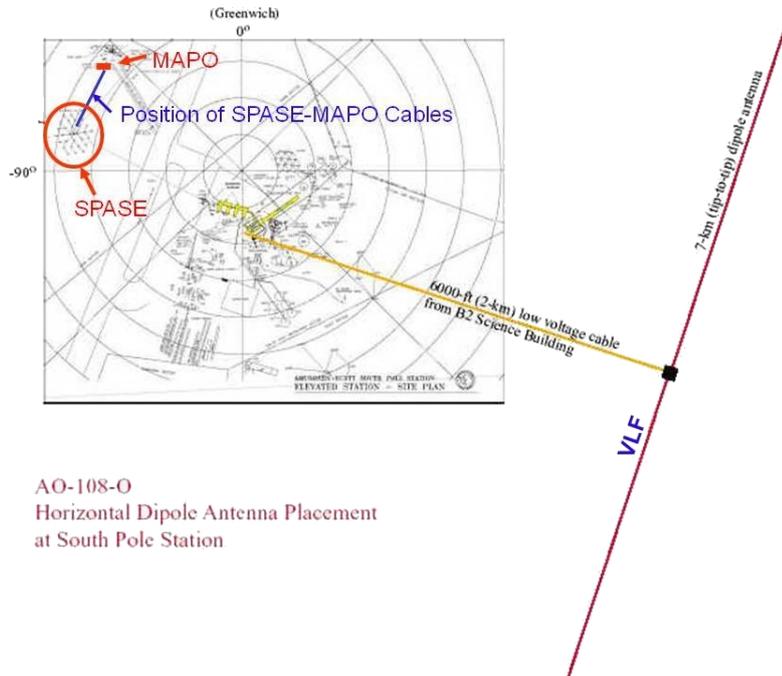
Figure 3.12: The Pole map of the VLF and the SPASE cables. These two cables run parallel to the VLF antenna, that makes them good antennas.

Figure 3.13: The VLF event on scope screen. The two waves are about 19 kHz. The yellow and red curve are the signals form the antenna cables to the SPASE building with the already removed antenna. The other curves are signals from 1m long open end cables.

of the experiment with the pole log book. The impact on the distribution is
low as seen in the graphs 3.6 and 3.9.

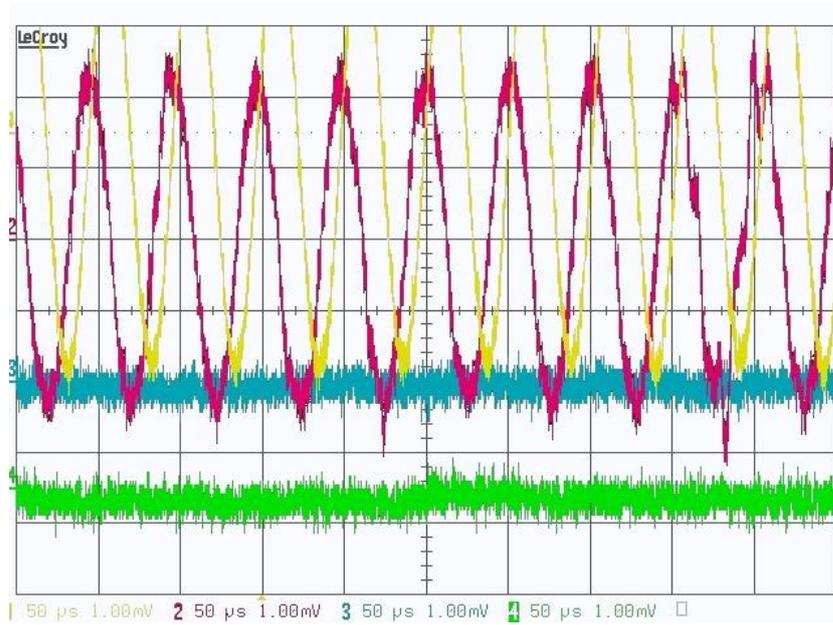| 'Pingerrun' arbitrary index	Log book date	'Pingerrun' day (missing waveform)
1	14:50, 20 January 2009 (CST)	no data = 20 Jan
2	13:07, 5 February 2009 (CST)	36 = 5 Feb
3	–	55 = 24 Feb
4	–	64 = 5 March
5	–	85 = 26 March
6	07:02, 6 April 2009 (CDT)	96 = 6 April
7	–	122 = 2 May
8	14:26, 24 April 2009 (CDT)	114 = 24 April
9	18 May	138 = 18 May
10	11:12, 26 May (CDT)	145 = 25 May
11	01:40, 5 June (CDT)	156 = 5 June
12	10:56, 9 July (CDT)	190 = 9 July
13	23:37, 15 July (CDT)	197 = 16 July

Table 3.1: Comparison of 'Pingerruns' times. This table shows the time,
taken from the AURA log book [33], when the surface horn antenna was
sending and compares it to the missing waveforms occurrences in the figure
3.7. In February and March there are not any entries in the log book. The log
book entries do not represent the correct sending time of the horn antenna,
but the time when the entry was made into the log book. The last entry is
at about midnight. This is why it was expected that the run would be at the
next day.

3.4.3   Radar

The meteor radar was built at the South Pole in 2001. Its purpose is mea-
suring the occurrence of small meteoroids by radar detection.

The meteor radar sends a 40μs pulse at 46.3 MHz. This pulse is sometimes
seen in the SPASE antenna's data. An example of this 46.3 MHz signal's
waveform with the according spectrum is shown in figure 3.14. The spectrum
of this shown waveform shows that the signal is at 46.3 MHz.

The occurrence of the meteor signal in the data is low. A filter for these
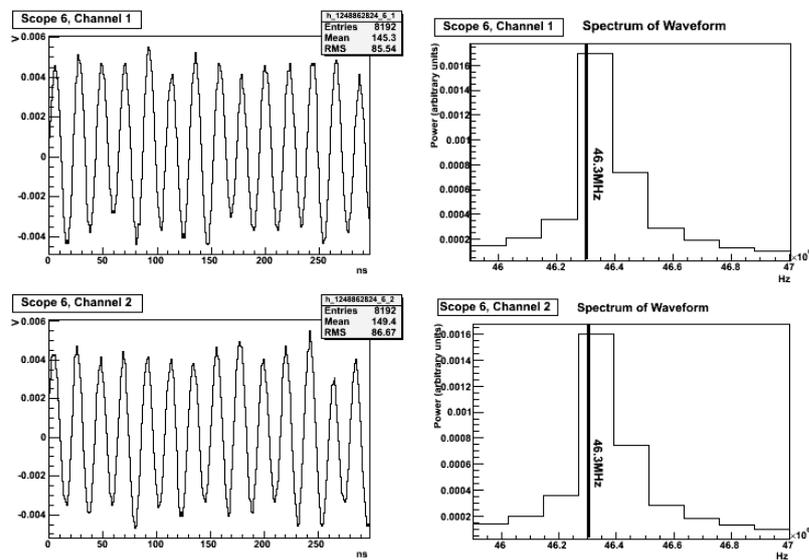signal was not developed.

Figure 3.14: Meteor Radar event. On the left, the waveform of a meteor radar pulse received by SPASE antennas is shown, on the right,the part of the spectrum is presented. The meteor radar pulse is at 46.3MHz.

Chapter 4

Modulation of minBias background events

A modulation of the standard deviation of the waveform voltages was found in the minBias background events. Figure 4.2 shows the modulation of the standard deviation for both SPASE antennas within a week.

4.1 Fit on the modulation of standard deviation

The standard deviation values are widely spread; the modulation has a sinusoidal shape but it is very difficult to apply a sinusoidal fit to it. This can be solved by reducing the variation induced by noise. This reducing is achieved by smoothing the data curve to fewer data points, whereas the smoothing is done by calculating the mean of the six standard deviation values, starting from the first data point up to the sixth data point. The next mean begins at the seventh data point and ends at the twelfth data point and so on. The standard deviation of these means has also to be calculated. And, as a result the fit can be done. Also, all data points below $4.36 \cdot 10^{-4} V_\sigma$ and above $7.28 \cdot 10^{-4} V_\sigma$ were ignored to filter meteor radar signals or signals resulting from connection problems and others before the mean was calculated.

This fit was done for a period of 18 weeks which started calendar week 21 and ended calendar week 39. Figure 4.2 shows the fit, also. The sinusoidal fit function is:

$$f(t) = A \sin\left(\frac{2\pi t}{T} + \phi\right) + D. \tag{4.1}$$

The resulting parameters are the amplitude $A = 1.78 \pm 0.06 \cdot 10^{-5} V_\sigma$, the period $T = 86184 \pm 11s$, the phase $\phi = 0.58 \pm 0.09$ and the offset $D =$

$6.07 \pm 0.01 \cdot 10^{-4} V_\sigma$. The fit result of parameter $T = 86184 \pm 11s$ is more or less a sidereal day ($86174s$). To exclude that this period of the fit correlates with a normal day period ($86400s$), this sinusoidal curve of a day's period is also drawn in figure 4.2. To show that a normal day period does not fit in this case. The fit results vary around the value of a sidereal day, because it is very difficult to apply a fit to background noise. However, it shows that a normal day period can be excluded.

The **sidereal day** is about 4 minutes shorter than a solar day. The sidereal day is defined as the interval between two successive upper culminations or transits of the vernal equinox [34]. Figure 4.1 shows that the Earth rotates about $361°$ on a mean solar day and $360°$ on a sidereal day. So a sidereal day is 4 minutes shorter than a solar day. However the vernal equinox precesses so that it is about 0.01 seconds less than defined with respect to the fixed point in space. A mean sidereal day is defined as $23^h 56^m 04^s.09054$ of universal time.

4.2   Reason for Modulation

The source of this modulation, due to the sidereal period of the background signal, could not come from our solar system. This modulation can be shown in a histogram. The histogram in figure 4.3 shows the modulation of the minBias events standard deviation V_σ in sidereal time. The sidereal time offset is set to the equinox at March 20th, 2008 5:48. Figure 4.4 shows the histogram of a normal day without modulation.

The Geographic South Pole lies on the rotation axis of the Earth, which intersects the Geographic North Pole and the Geographic South Pole. The stars rotate more or less around the rotation axis of the Earth. This is why the stars move around the Geographic South Pole in a sidereal day. The sources of the signals should rotate by $360°$ per a sidereal day , if these are outside our solar system. In a sidereal hour these sources move about $15°$ to the west. For example there is a source at 0 o'clock in the north that will be in the west at 6 o'clock.

There may be radio sources at 45 MHz in the galactic plane, seen in the 45MHz radio continuum survey [35]. The galactic plane emits most of its radio emission around the galactic center. Along the galactic plane the sources are spread about $45°$ in length and $30°$ in width - seen from the center. For tracking the galactic plane, the galactic center located with the star (SAGITTARIUS A*) at the sky is used for locating. A plot from kstar [36] program shows the galactic plane at 0 o'clock in north direction, see figure 4.5. The galactic center is $29°$ above the horizon in the north.

Figure 4.1: Motion of earth in 1 sidereal day and in 1 solar day. The Earth have to rotate 361° for a solar day. To see the same point on the sky the Earth have to rotate 360°. The Earth needs a little less as 4 minutes for 1° of rotation. Graphic has been taken from [34].

The stars on the sky rotate at the Geographic South Pole counter-clockwise around the rotation axis of the Earth.

The figures 4.7 and 4.8 show polar plots of a sidereal day. These plots give the signal strength variation in sidereal time. A possible explanation for the variation is that, maybe, the radio signals are blocked by the SPASE2 building, which is located near the antennas. Figure 4.6 shows the locations of antennas and the building. The polar plots are included as well. In 4.6, there is a building between the antennas and the source. The distance form SPASE1 to the building measures about 40 feet or 12m, the height of the building is about 6m. The galactic center is about 29° above the horizon, but it is also above the building. If the galactic plane crosses between the antenna and the SPASE building, the signal is reduced because a fraction of the signal from the galactic plane is blocked by this building. For the SPASE2 antenna which is nearer the building, the signal strength modulation is stronger.
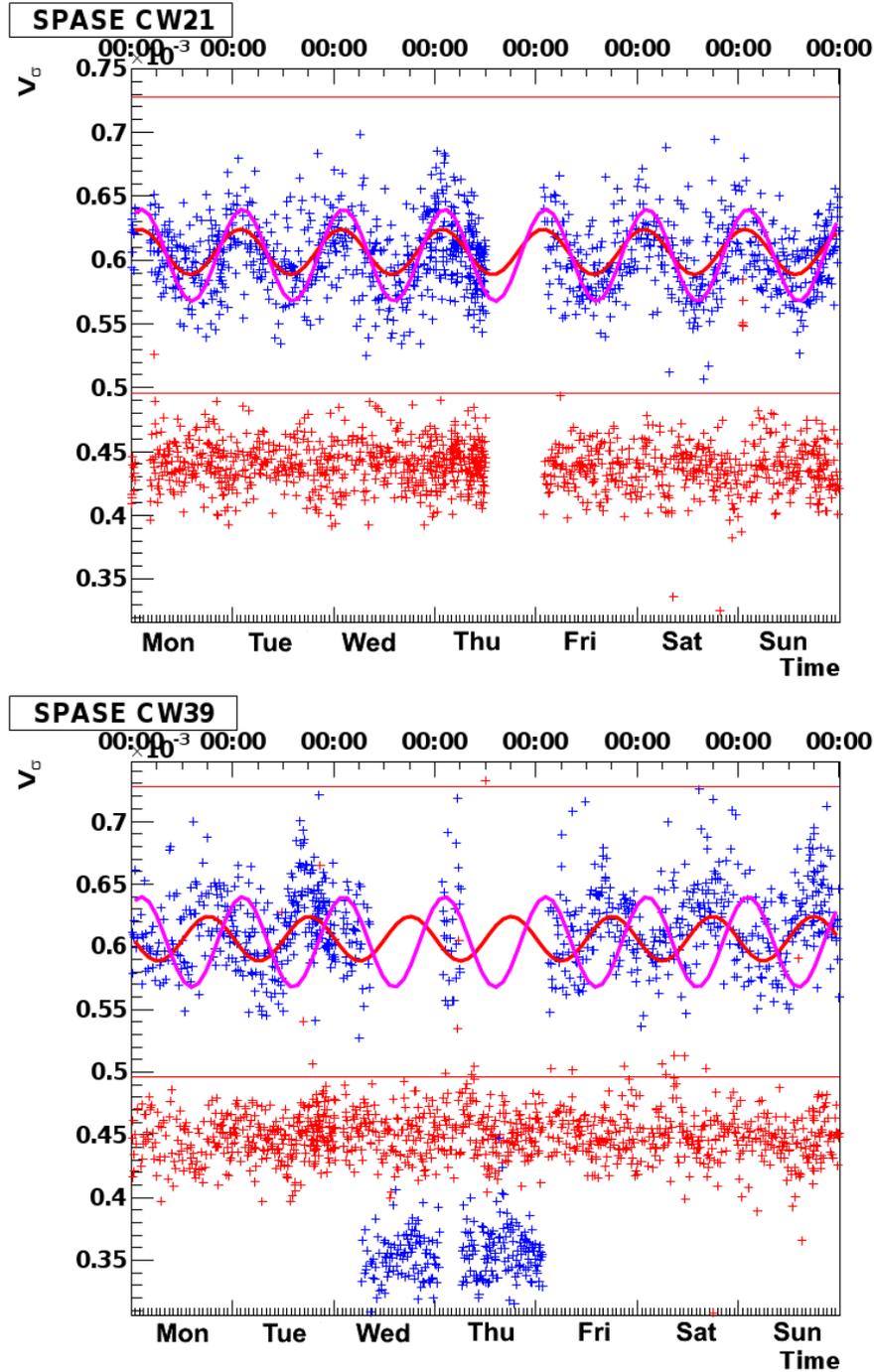
Figure 4.2: Fit over a period of 18 weeks. The plane displayed above shows the first week and the plane below shows the last week of the fit. The blue crosses are the standard deviation V_σ of the SPASE2 antenna minBias events and the red crosses are the standard deviation V_σ of SPASE1 antenna minBias events. The magenta line is the day period (86400s) of a sinusoid and the the red line is a fit with a period of $86184 \pm 11s$. As the two sinusoidal function do not coincide, we can conclude that the modulation does not correspond to a source from the solar system.
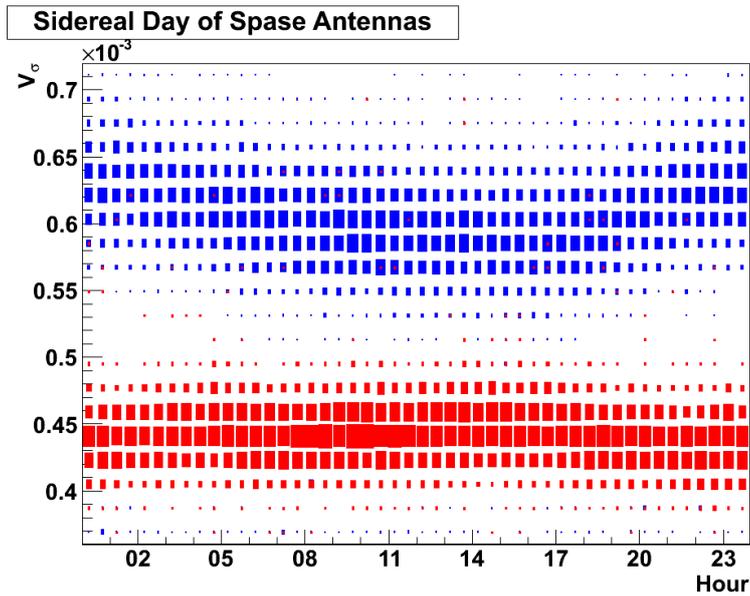
Figure 4.3: Histogram of a sidereal day. The blue boxes are standard deviations V_σ of the minBias events from the SPASE2 antenna and the red boxes are standard deviations V_σ of the minBias events from the SPASE1 antenna. The distribution of the blue boxes shows clearly a modulation of the signals received by the SPASE2 antenna. The distribution of the red boxes shows only very weak modulation received by the SPASE1 antenna.
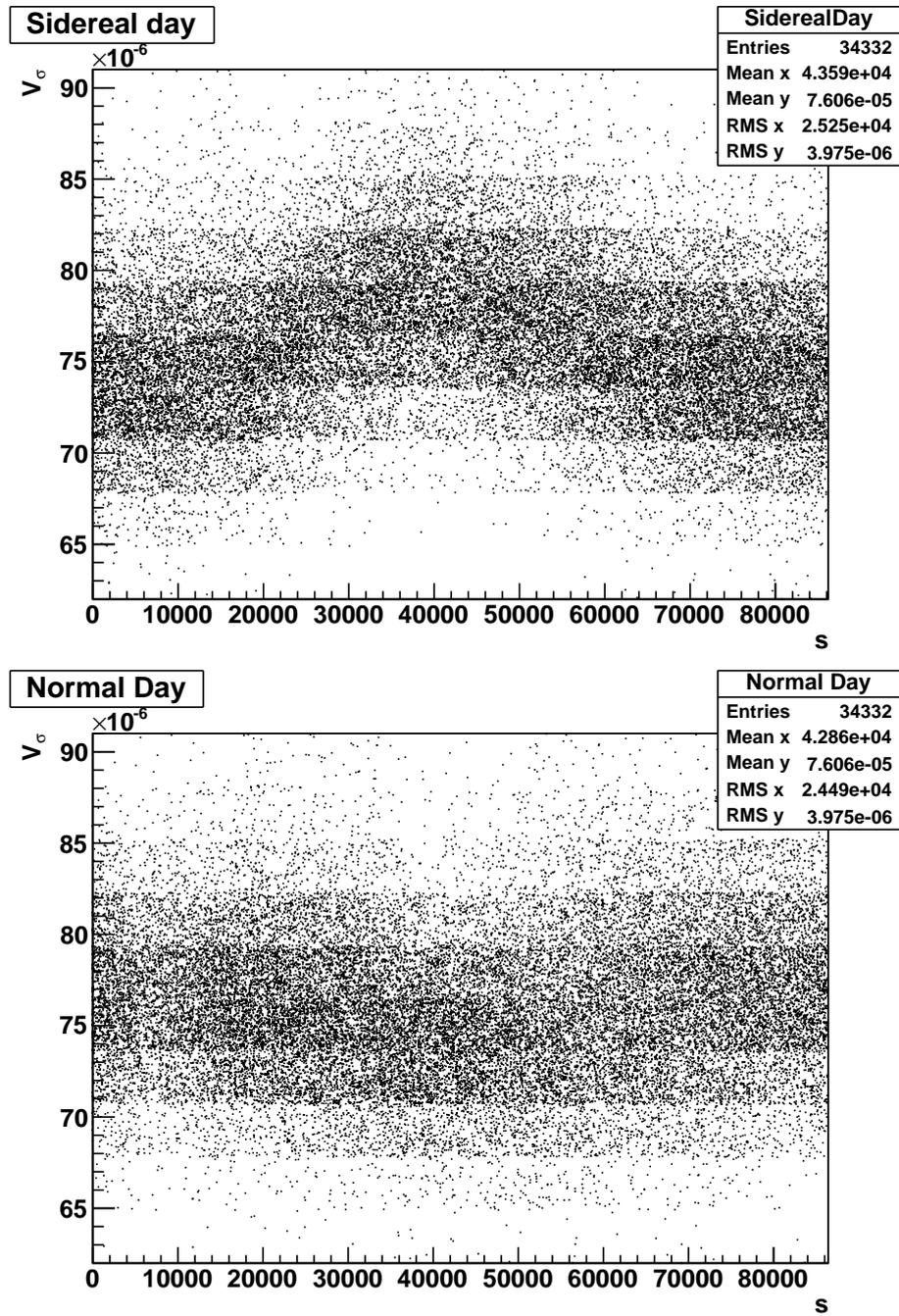
Figure 4.4: Comparison of a normal and a sidereal day histogram. The panel above shows the sidereal day period and the panel bellow shows the normal day period.
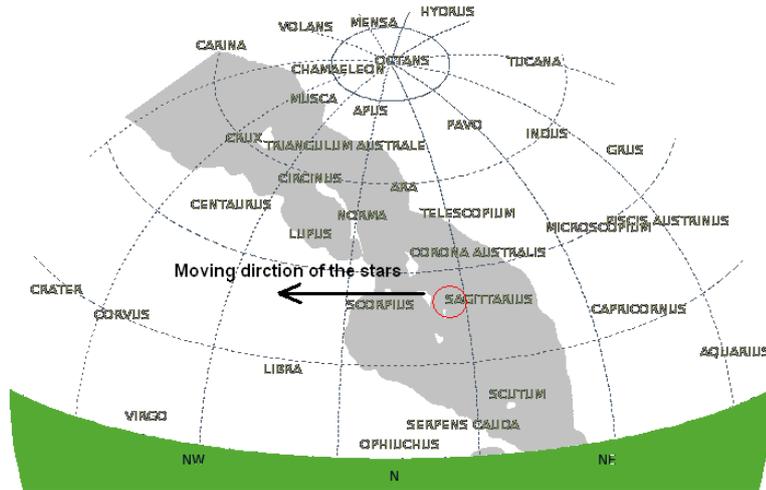
Figure 4.5: View of the sky in the north March 20th, 2008 5:48. The galactic center is located in the Sagittarius constellation. The stars move to the left.
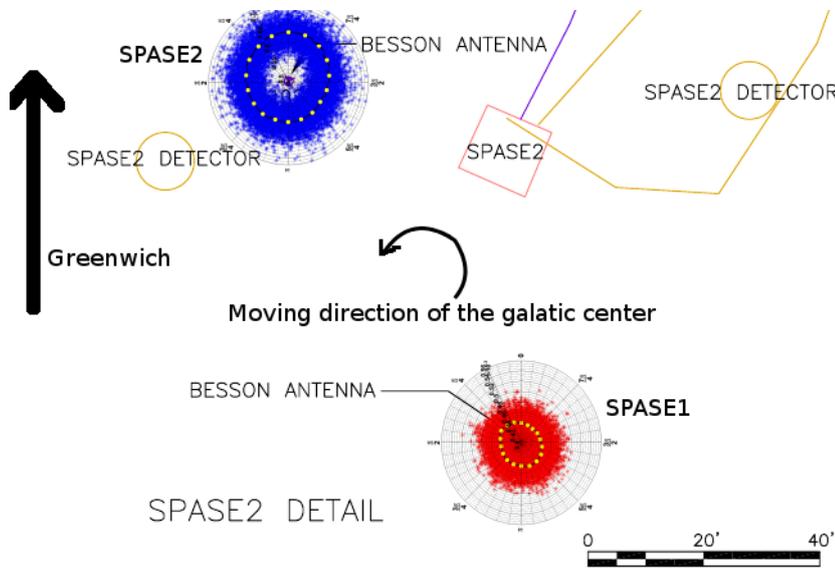

Figure 4.6: Map of the SPASE antennas at the SPASE2 building. The polar plots are put on the antenna positions. These plots show the sidereal time variation of the signal. The signal is weaker when the building is between the galactic center and the antenna.
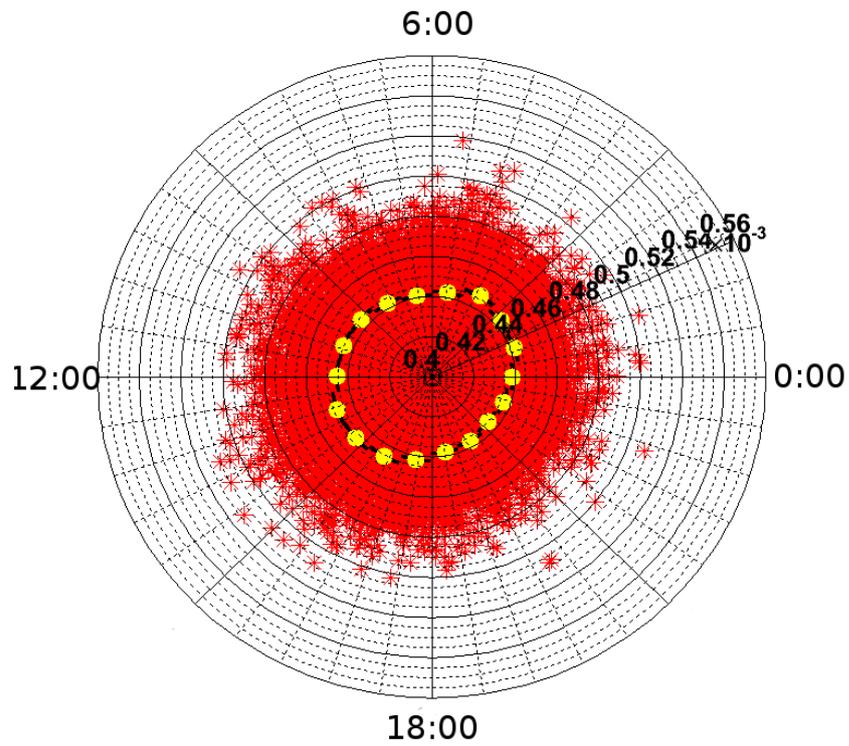
Figure 4.7: Polar plot of the V_σ of the SPASE1 antenna. A sidereal day is 360° with 1° corresponding 4 sidereal minutes. The standard deviation is smaller than the yellow dots shown, so they cannot be seen.

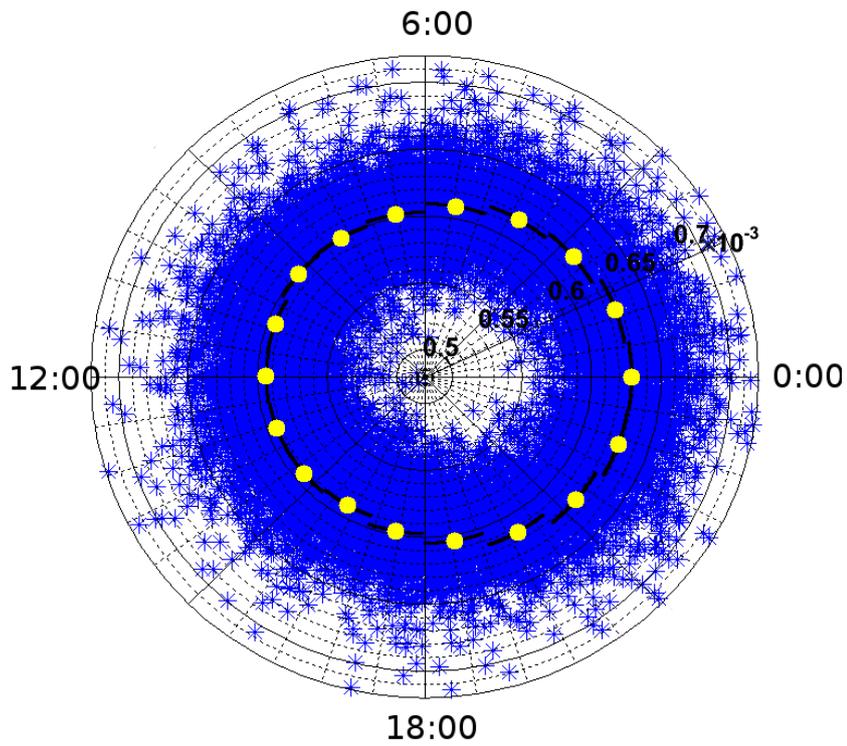Figure 4.8: Polar plot of the V_σ of the SPASE2 antenna. A sidereal day is $360°$ with $1°$ corresponding 4 sidereal minutes. The standard deviation is smaller than the yellow dots shown, so they cannot be seen.

Chapter 5

Summary and Outlook

At the current development status of the fat wire dipole (FWD) antenna not all features have been simulated and measured yet. The VSWR and the direction pattern have already been simulated, but one feature the dispersion of the antenna signals, is still missing, which is being researched by Markus Vehring [37]. Currently, only the VSWR has been measured with good results in the designed frequency range from 25 MHz to 120 MHz. Owing to the complexity of the measurements the direction pattern is missing. A second, calibrated antenna for this measurement is required. The measurement of the dispersion has not been done until now.

In total, 8 antennas were built in Wuppertal, two prototypes and another 6 meant for deployment at the South Pole. These antennas will have to be used in the Radio Air Shower Test Array (RASTA), because they are currently the best known for this purpose. This experiment is expected to take place in 2010/2011 or 2011/2012.

The two existing antennas have been providing material to study the background noise. The event number and ADC conversion factor have already delivered interesting results, which are useful to filter invalid events:

The first result was the possibility to prove the integrity of the data by checking the event numbers' sequence.

The second one was the wrong dynamic range of events with an event number equal to 1.

The research on the standard deviation of the waveforms of the minBias events has shown that the most events above the normal background noise level are mostly VLF events.

The pinger runs, too, could be clearly identified. The SPASE2 antenna also had some problems with its connections.

A further unexpected effect,the sidereal time modulation of the standard deviation of the waveforms, was caused by the building in proximity of the

antennas, as it shadows the signals from the area around the galactic center.

In conclusion we can say that the major background noise sources have now been identified, which were discussed in this thesis. Yet, more experience to be carried out in future will offer an even better understanding of this field of research.

Hiermit versichere ich, dass ich diese Arbeit selbstständig verfasst und keine anderen als die angegebenen Hilfsmittel und Quellen benutzt sowie Zitate kenntlich gemacht habe.

Wuppertal den 16.8.2010

Andreas Schultes

Bibliography

[1] V.F. Hess. Über beobachtungen der durchdringenden strahlung bei sieben ballonfahrten. *Phys. Zeitschr. 13*, pages 1084–1091, 1912.

[2] W. Kohlhörster. *Phys. Zeitschr. 26*, page 654, 1925.

[3] P. Auger et al. *Comptes rendus 206*, page 1721, 1938.

[4] W. Kohlhörster et al. *Naturw. 26*, page 576, 1938.

[5] G. Kulikov and G. Khristiansen. *JETP 35*, page 635, 1958.

[6] J. Linsley. *Proc. 8th ICRC Jaipur India*, pages 77–99, 1963.

[7] J. Linsley. *Proc. 8th ICRC, Jaipur, India*, pages 77–99, 1963.

[8] Kenneth Greisen. End to the cosmic-ray spectrum? *Phys. Rev. Lett.*, 16(17):748–750, Apr 1966.

[9] A. A. Penzias and R. W. Wilson. A Measurement of Excess Antenna Temperature at 4080 Mc/s. *apj*, 142:419–421, July 1965.

[10] HiRes Collaboration. First observation of the greisen-zatsepin-kuzmin suppression. *Phys. Rev. Lett.*, 100, 2008.

[11] M. Takeda et al. Energy determination in the akeno giant air shower array experiment. *Astropart.Phys.*, 19:447–462, 2008.

[12] M. Takeda et al. Observation of the suppression of the flux of cosmic rays above $4x10^19ev$. *Physical Review Letters*, 2008. arXiv:0806.4302v1.

[13] R. Engel J. Blümer and J.R. Hörandel. Cosmic rays from the knee to the highest energies. *Prog. Part. Nucl. Phys. arXiv:0904.0725v [astro-ph.HE]*, 2009.

[14] T.K. Gaisser and A.M. Hillas. Reliability of the method of constant intensity cuts for reconstructing the average development of vertical showers. page 353, Plovdiv, Bulgaria, 1977.

[15] The Auger Collaboration. The pierre auger observatory design report. Technical report, 2nd edition, 1997.

[16] Suling M. Bürger j., Böhm E. Energy spectra and production height of mouns in eas. pages 2784–+, 1975.

[17] Steffen Nehls. *Calibrated Measurements of the Radio Emission of Cosmic Ray Air Showers.* PhD thesis, Forschungszentrum Karlsruhe Institut fÃ¼r Kernphysik, 2008.

[18] *Classical Electrodynamics Third Edition.* John Wiley & Sons, Inc., 1999.

[19] T. Huege and H. Falcke. *A&A*, (19):412, 2003.

[20] Corsika an air shower simulation program. http://www-ik.fzk.de/corsika/.

[21] N. A. Porter T. C. Weekers F. G. Smith J. V. Jelley, J. H. Fruin and R. A. Porter. *Nature*, 205:327, 1965.

[22] Jan Auffenberg. *On a prototype detector for the radio emission from air showers at the South Pole.* PhD thesis, Bergische UniversitÃ¤t Wuppertal, 2010.

[23] Icecube neutrino observatory.

[24] The rasta proposal. intern.

[25] G. J. Burke and A. J. Poggio. Numerical electromagnetic code 2. Technical report, Lawrence Livermore Laboratory, 1981.

[26] S A. Arcone A. J. Delaney and J. H. Rand. Radar investigations of proposed utilidor sites at south pole station. 1999.

[27] G.A. Askarayan. Coherent radio emission from cosmic showers in air and in dense media. *JETP*, 21:658, 1965.

[28] I. Kravchenko. Event reconstruction and data acquisition for the rice experiment at the south pole. Technical report, MIT, 2007.

[29] Root. http://root.cern.ch.

[30] Umran S. Inan. Standford very low frequency beacon. http://nova.stanford.edu/ vlf/south$_p$ole/southpole.htm.

[31] M. W. Chevalier, W. B. Peter, U. S. Inan, T. F. Bell, and M. Spasojevic. Remote sensing of ionospheric disturbances associated with energetic particle precipitation using the South Pole VLF beacon. *Journal of Geophysical Research (Space Physics)*, 112(A11):11306–+, November 2007.

[32] unknown. Standford very low frequency beacon transmission stratagy. Ice-Cube wiki document.

[33] Hagar. Aura pole log book 1. IceCube wiki document.

[34] *Radio Astronomy*. McGraw-Hill Book Company, 1966.

[35] J. May H. Alvarez, J. Aparici and F. Olmos. A 45-mhz continuum survey of the southern hemisphere. *Astron. Astrophys. Suppl.*, (124):315–328, 1997.

[36] Kstars desktop planetarium for kde. http://edu.kde.org/kstars/.

[37] Markus Vehring. Private communications.

[38] Edmund Stirnr. *Antennen Band 1: Grundlagen 2. durchgesehene Auflage.* Dr. Alfred Hüthig Verlag GmbH Heidelberg, 1977.

[39] Edmund Stirnr. *Antennen Band 2: Praxis 2. durchgesehene Auflage.* Dr. Alfred Hüthig Verlag GmbH Heidelberg, 1977.

[40] G. Dubost and S. Zisler. *Breitband-Antennen Theorie und Anwendung.* R. Oldenbourg Münschen Wien, 1976.

[41] Edward A. Wolff. *Antenna analysis.* Artech house Inc., 1988.

[42] Karl Rothhammel. *Rothammels Antennenbuch.* DARC Verlag Baunatal, 2002.

[43] Lothar Sachs. *Angewandte Statistik.* Springer-Verlag GmbH, 2002.